

Metal–Halide Perovskite Nanocrystal Superlattice: Self-Assembly and Optical Fingerprints

Zhuang Liu, Xian Qin,* Qihao Chen, Tianci Jiang, Qiushui Chen, and Xiaogang Liu*

Self-assembly of nanocrystals into superlattices is a fascinating process that not only changes geometric morphology, but also creates unique properties that considerably enrich the material toolbox for new applications. Numerous studies have driven the blossoming of superlattices from various aspects. These include precise control of size and morphology, enhancement of properties, exploitation of functions, and integration of the material into miniature devices. The effective synthesis of metal–halide perovskite nanocrystals has advanced research on self-assembly of building blocks into micrometer-sized superlattices. More importantly, these materials exhibit abundant optical features, including highly coherent superfluorescence, amplified spontaneous laser emission, and adjustable spectral redshift, facilitating basic research and state-of-the-art applications. This review summarizes recent advances in the field of metal–halide perovskite superlattices. It begins with basic packing models and introduces various stacking configurations of superlattices. The potential of multiple capping ligands is also discussed and their crucial role in superlattice growth is highlighted, followed by detailed reviews of synthesis and characterization methods. How these optical features can be distinguished and present contemporary applications is then considered. This review concludes with a list of unanswered questions and an outlook on their potential use in quantum computing and quantum communications to stimulate further research in this area.

1. Introduction

Self-assembly of microscopic building blocks into mesoscopic or even macroscopic aggregates with highly ordered orientations mimics nature's problem-solving ability.^[1] Nanocrystals dispersed in a solution can self-align and form superlattices due to the balance between attractive and repulsive forces. Compared to their monomers, the properties of ordered superlattices are quite distinct, as the structural hierarchy and compositional versatility confer novel electrical, mechanical, optical, magnetic, and catalytic functionalities to these aggregates (Figure 1).^[2–12]

Beginning with the first single-component CdSe superlattices in 1995 (Figure 2a) and culminating with the discovery of multiple-layer SiO₂ superlattices in 1999 (Figure 2b), the diversity of inorganic nanocrystal superlattices has been significantly enriched by versatile synthetic methods readily available for high-quality superlattices.^[13–17] These superstructures with atomic precision continue to motivate research on novel superlattices. Almost a decade after the discovery of CdSe superlattices, the development of multicomponent superlattices has been hampered by

the difficulty of balancing nanoscale interactions such as van der Waals forces, electrostatic effects, steric repulsion, molecular dipole interactions, and hydrogen bonding.^[18] In 2002, Fe₂O₃ nanocrystals and PbSe quantum dots self-assembled into highly ordered 3D binary nanocrystal superlattices with unprecedented high packing density (Figure 2c).^[15] Since then, over 15 types of binary nanocrystal superlattices have been exploited, spanning a broad range of materials, including semiconducting, metallic, and magnetic building blocks (Figure 2e).^[16] Moreover, in-depth studies have proven that the stoichiometry of binary nanocrystal superlattices is mostly dictated by electric charges on sterically stabilized nanocrystals, with lesser contributions from entropic, van der Waals, steric, and dipolar forces. In 2003, packing models were proposed to explain the structural configurations of superlattices and predict possible arrangements (Figure 2d).^[19]

Recent advances in microscopic force manipulation have led to the assembly of superlattices with intriguing orientational patterns and structural configurations. For example,

Z. Liu, X. Liu
Joint School of National University of Singapore and Tianjin University
International Campus of Tianjin University
Binhai New City, Fuzhou 350207, China

Z. Liu, X. Qin, X. Liu
Department of Chemistry
National University of Singapore
Singapore 117543, Singapore
E-mail: chmqinx@nus.edu.sg; chmlx@nus.edu.sg

Q. Chen, T. Jiang, Q. Chen
MOE Key Laboratory for Analytical Science of Food Safety and Biology
Fujian Provincial Key Laboratory of Analysis and Detection
Technology for Food Safety
College of Chemistry
Fuzhou University
Fuzhou 350002, China

 The ORCID identification number(s) for the author(s) of this article can be found under <https://doi.org/10.1002/adma.202209279>.

DOI: 10.1002/adma.202209279

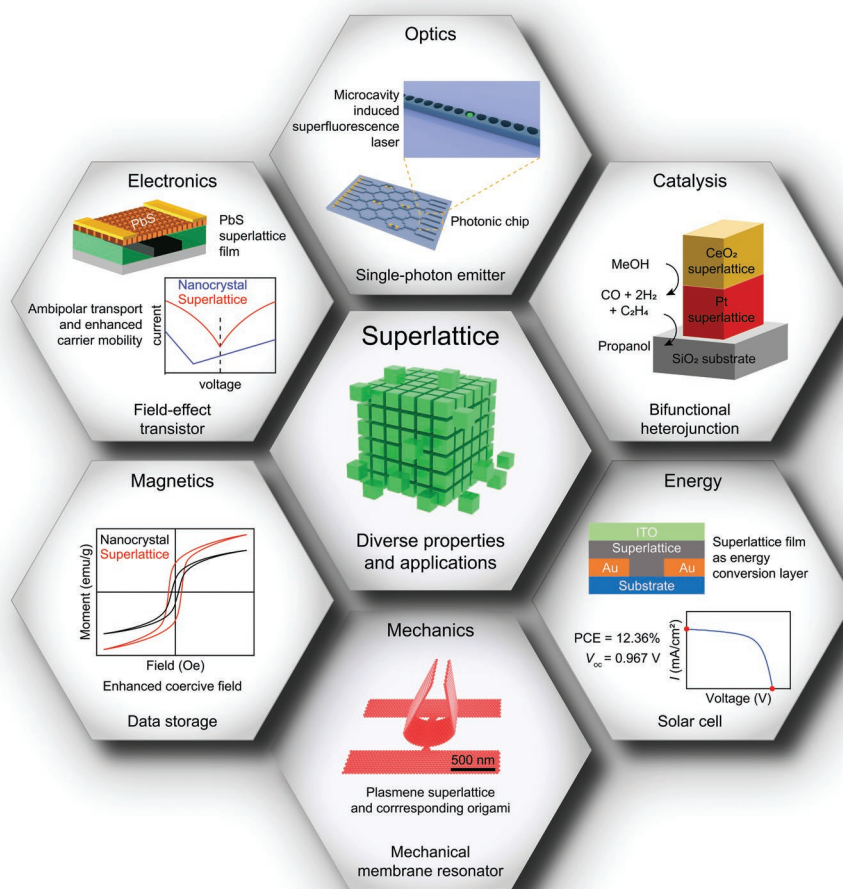


Figure 1. Diverse properties and emerging applications of superlattices.

self-assembly of isotropic Fe_3O_4 nanocrystals into 1D, highly ordered superlattices was achieved using PbSO_4 -oleate complexes as templates, in which dispersed nanocrystals were encapsulated by a half-cylindrical cluster shell (Figure 2g).^[20] Using this method, the superlattice length approached $\approx 20 \mu\text{m}$. Surprisingly, nanocrystals with identical chemical compositions self-assembled into helical arrays by carefully controlling growth conditions (Figure 2f).^[21] The formation of helical superlattices was governed by the interplay between van der Waals forces, magnetic dipole–dipole interactions, Zeeman coupling, and entropic forces, as revealed by Monte Carlo simulations. This finding has provided unique insights into the mechanism of symmetry breaking and chirality amplification.

Since the inception of hybrid perovskite nanocrystals (MAPbBr_3 , MA: CH_3NH_3) and their all-inorganic counterparts (CsPbX_3 , X: Cl, Br, or I), metal–halide perovskite nanocrystals have become star materials due to their exceptional properties, including large radiation absorption, bright excitonic emission, tunable bandgaps, and high tolerance to structural defects.^[22–28] Compared to nanocrystals, bulky perovskites usually exhibit low photoluminescence quantum yield (PLQY) due to the long diffusion length of photogenerated charge carriers.^[29] As

with conventional GaAs superlattices and CdTe aggregates, researchers have demonstrated that the assembly of perovskite nanocrystals into superstructures can effectively shorten charge carrier diffusion distances.^[30–32] The electronic coupling between nanocrystal units leads to the formation of minibands in both valence and conduction bands, suppressing nonradiative recombination of charge carriers at defect sites and facilitating excitonic radiative decay.

Breakthroughs in self-assembly and superlattices are rewarding. Using a drying-mediated self-assembly method, ensembles of monodisperse cuboidal CsPbBr_3 nanocrystals readily formed superlattices with slightly enhanced stability compared with dispersed nanocrystals.^[30,33–46] Under optimized preparation conditions, clusters of nanocrystals can assemble into a cuboidal superlattice that can reach a length of $10 \mu\text{m}$ (Figure 2h).^[30,47] These superlattices exhibited unique optical features, such as coherent superfluorescence, increased stimulated emission, and a significant redshift of the spectrum, which was attributed to quantum confinement of charge carriers by the quantum-well-like superlattices. In the case of superfluorescence, this particular optical characteristic is due to the rapid coherence of all nanocrystal components in a single

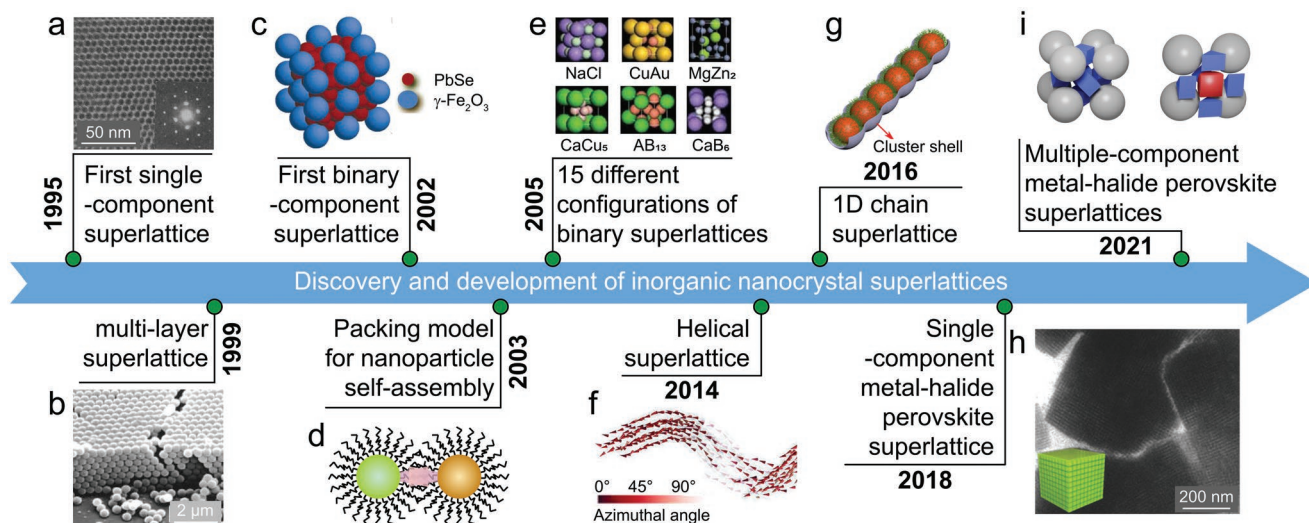


Figure 2. Evolution of inorganic nanocrystal superlattices. a) High-resolution transmission electron microscopy (HRTEM) image of the CdSe superlattices. Inset is the corresponding small-angle electron diffraction pattern. b) Scanning electron microscopy (SEM) cross-sectional images of SiO₂ superlattices with seven layers. c) Schematic of binary superlattices comprising PbSe and Fe₂O₃ nanocrystals. d) Schematic of optimal packing model. e) Unit cells of different binary superlattices. f) Simulation depicting the folding of a 1D Fe₃O₄ belt into a helix superlattice. g) Schematic of 1D Fe₃O₄ superlattice assembled using a molecular cluster shell. h) HAADF-STEM image of a single superlattice of CsPbBr₃ nanocrystals. i) Schematic of multiple-component metal-halide perovskite superlattices. (a) Reproduced with permission.^[13] Copyright 1995, AAAS. (b) Reproduced with permission.^[14] Copyright 1999, American Chemical Society. (c) Reproduced with permission.^[15] Copyright 2003, Springer Nature. (e) Reproduced with permission.^[16] Copyright 2006, Springer Nature. (f) Reproduced with permission.^[21] Copyright 2014, AAAS. (g) Reproduced with permission.^[20] Copyright 2016, American Chemical Society. (h) Reproduced with permission.^[30] Copyright 2018, Wiley-VCH. (i) Reproduced with permission.^[49] Copyright 2021, Springer Nature.

superlattice under a collective light field.^[48] This optical phenomenon was also observed in multicomponent nanocrystal superlattices composed of other inorganic nanoparticles (Figure 2i).^[49] As a result, possibilities exist for metal-halide perovskite superlattices as quantum light sources, which are anticipated to be used for Boson sampling, quantum communication, and photonic quantum computing.^[50–52]

This review aims to discuss multiple aspects of metal-halide perovskite superlattices. In Section 2, we begin with three classic packing models to explain the stacking configurations of superlattices. We then describe the major impact of capping ligands on superlattice stability, typical synthetic methods for preparing superlattices, and characterization techniques commonly used to identify nanoscale structures at the molecular level. In Section 3, their unique photophysical mechanisms and optical properties, including superfluorescence, amplified spontaneous emission, and spectral redshift, are discussed. Section 4 introduces their application possibilities as quantum light sources and solid-state light emitters. This review concludes with open questions, challenges, and further development perspectives.

2. Fundamental Considerations

2.1. Packing Models

Typical packing models for nanocrystal superlattices can be used to virtually construct metal-halide perovskite superlattices, particularly multicomponent systems with extremely high packing densities.^[19,53–59] By tuning model parameters, broadly

applicable theoretical models can predict unknown packing configurations. For example, there are three packing models, namely the optimal packing model (OPM), orbifold topological model (OTM), and overlap cone model (OCM), depending on how ligand chains coordinately passivate nanocrystal cores. These models compare well with molecular dynamics simulations and experiments to a great extent. By way of illustration, in ABO₃-type superlattice self-assembled from perovskite nanocrystals and other inorganic nanoparticles, the measured packing density is slightly higher than the predicted packing fraction, mainly due to the deformation of capping ligands.^[49,60,61]

It has been demonstrated that the basic symmetry of a given superlattice is determined by a parameter x , defined as the ratio of the ligand chain length L to the nanocrystal radius R .^[19] Note that L and R measure in nanometers. A crossover of x between the face-centered cubic (fcc) and body-centered cubic (bcc) phases has been widely observed. In general, a smaller x often leads to a fcc structure as short-chain ligands cannot completely fill the superlattice, while long-chain ligands yield a higher x and extend to or even interact directly with neighboring ligands, resulting in a bcc phase.^[62] Considering that the atomic usage efficiency in a fcc unit cell is 0.74, which is higher than 0.68 in a bcc structure, a larger packing degree is likely to be achieved in fcc superlattices where short-chain ligands are widely employed.^[63] Based on the geometric principles, a hard-sphere model, known as the OPM, was then developed as the first prototype to describe the correspondence between 3D geometric configuration and packing arrangement in nanocrystal superlattices (Figure 3a).^[19,64,65]

In an ideal OPM, two identical nanocrystal cores are coordinated by ligand chains and exhibit a symmetric pattern. Note

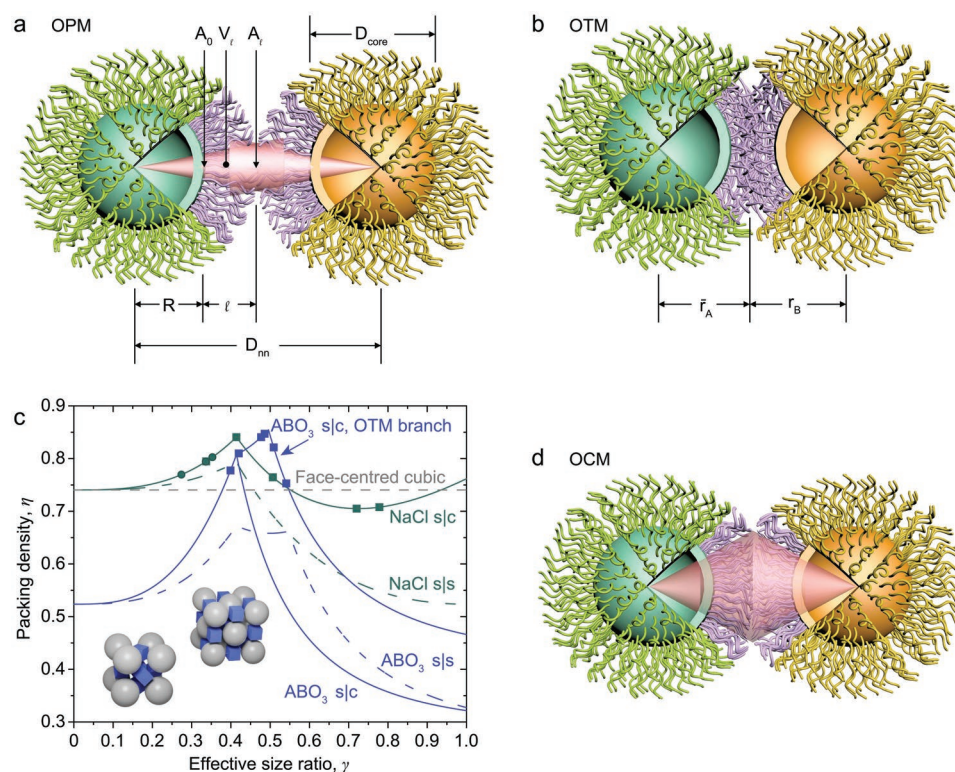


Figure 3. Three packing models for superlattice construction. a) Optimal packing model (OPM). b) Orbifold topological model (OTM). c) High packing density in metal–halide perovskite superlattices. d) Overlap cone model (OCM). (c) Reproduced with permission.^[49] Copyright 2021, Springer Nature.

that the chain head groups anchored on nanocrystal surfaces occupy a characteristic area A_0 and generate a circular pattern on the surface. A virtual cone with a length of $R + L$ is then formed by linking the core center and the circular pattern. Considering that the ligands can penetrate their neighbors to form a shared plane at the position $L = l$, the volume of the circularly truncated cone is defined as V_l .^[64] Similar to the definition of $x = L/R$, x_l and A_l at the position $L = l$ can be calculated accordingly. With these definitions, V_l is given by

$$V_l = A_0 l (1 + x_l + x_l^2 / 3) \quad (1)$$

Considering the symmetry of two-particle system, the distance l equals half of the distance between two nanocrystal cores, namely $l = (D_{nn} - D_{core})/2$. Then, Equation (1) can be rewritten as

$$V_l = \lambda V_0 \quad (2)$$

where $V_0 \equiv A_0 l$ and the scaling factor λ is a geometry-dependent parameter close to unity. By combining Equations (1) and (2), the real root is obtained as

$$x_l = (1 + 3\lambda x)^{1/3} - 1 \quad (3)$$

After substitution of $l = (D_{nn} - D_{core})/2$, Equation (3) is then expressed as

$$D_{nn} = D_{core} (1 + 3\lambda x)^{1/3} \quad (4)$$

Given that a bcc structure has a lower space-filling efficiency than a fcc structure, nanocrystals are inclined to self-assemble into bcc superlattices. In this regard, the short-chain ligands cannot reach their next nearest neighbors in the bcc phase. Hence D_{nnn} is calculated as

$$D_{nnn} \equiv 2D_{nn} / \sqrt{3} = D_{core} + 2L \quad (5)$$

Combining Equations (4) and (5), the λ can be correlated with x_B by

$$(2/\sqrt{3})(1 + 3\lambda x_B)^{1/3} = 1 + x_B \quad (6)$$

where the subscript B stands for phase boundary between bcc and fcc arrangements. Note that the fcc lattice has a smaller x ($x < x_B$), while the bcc lattice possesses a larger x ($x > x_B$). Therefore, the core volume fractions for bcc and fcc lattices are obtained as

$$V_{bcc} = \pi(\sqrt{3}/8)/(1 + 3\lambda x) = 0.68(1 + 3\lambda x) \quad (7a)$$

$$V_{fcc} = \pi/(3\sqrt{2})/(1 + 3\lambda x) = 0.74(1 + 3\lambda x) \quad (7b)$$

The coefficients of 0.68 and 0.74 are the space-filling efficiencies in bcc and fcc lattices, respectively. Note that two nanocrystals directly touch each other when $x = 0$.

Generally, OPM uses information on nanocrystal size, ligand type, and local symmetry to construct superlattices, and the

configurations predicted by OPM usually agree to some extent with experimental results.^[19,62] However, nanocrystals are not as “hard” as assumed in OPM, which is considered the main shortcoming of this model. The equilibrium between multiple nanoscale forces, including van der Waals forces, electrostatic effects, steric repulsion, molecular dipole interactions, and hydrogen bonding, endows a “soft” feature on individual nanocrystals and their assemblies.^[18] Moreover, superlattices with long-chain ligands are “softer” than those with short-chain ligands, resulting in a nontrivial deviation from experimental results. To include the deformation of ligand chains in the OPM, an improved OTM has been proposed to better describe superlattice configurations.^[57–59]

Unlike the OPM with the maximum ligand packing density, the OTM assumes a short distance between nanocrystals.^[57] The rationale for this assumption is that ligand chains are soft and can tolerate mechanical deformation to a certain degree (Figure 3b). In addition, the maximum length L of capping ligands in OTM depends on the chemical composition. Another feature of OTM is to consider the influence of topological defects that arise during ligand deformation.^[58] Given that the degree of deformation depends on the chain length, ligands with n saturated hydrocarbons are considered representative, and their length L is given as

$$L = nr_0 \cos(\alpha/2) + r_1 = 0.128n + 0.2 \quad (8)$$

where $\alpha = 180^\circ - 112^\circ = 68^\circ$ is the C–C angle, $r_0 = 0.154$ is the C–C bond length, and $r_1 = 0.2$ is the radius of each terminal carbon atom.^[66]

OTM can explain unprecedentedly high packing fractions in binary fcc superlattices composed of metal–halide perovskite nanocrystals and other inorganic nanoparticles.^[49] The packing density of 0.85 is higher than the maximal packing density of 0.74 predicted in the fcc phase. Considering that building blocks are usually spherical and cubic nanocrystals, the packing density correlates with the shape chosen for modeling.^[49] For instance, OTM-based modeling has shown that the packing density of superlattices with both spherical and cubic configurations of the ABO_3 -type is slightly higher than that of the NaCl-type counterparts. By contrast, modeling based on pure spheres suggested a lower packing density of the ABO_3 -type configuration (Figure 3c). It is worth noting that in superlattices composed of spherical and cubic nanocrystals, both ABO_3 - and NaCl-type fcc lattices possess high packing fractions, exceeding the largest packing density in the fcc arrangement. This anomaly was attributed to the structural deformation of capping ligands, whose chains are highly malleable and can fill irregular voids in the superlattices to a large extent.

Despite the improved prediction precision, OTM showed a significant deviation from experiments when applied to nanocrystals with coordination numbers less than six.^[57] Notably, OTM has been shown to be unable to describe CaB_6 , CsCl, and Li_3B configurations. To address these issues, a revised model, named the OCM, was constructed by neglecting the interaction between ligands in the packing area (Figure 3d).^[53–56] Specifically, ligand chains fill the space within the overlapped region, indicating a shorter distance between nanocrystals than

OPM and OTM. This model proved to be useful for predicting nanocrystal packing in CsCl and CaB_6 configurations.

2.2. Capping Ligands

In Section 2.1, contributions from saturated hydrocarbons ligand chains were analyzed in OTM, showing that their characteristics such as length, head or end groups, and bond angles in different chemical bonds have a considerable impact on the final orientation of the superlattice. In fact, prior studies have proved that the categories and loading concentrations of capping ligands largely determine the quality and geometries of self-assembled superlattices.^[1,2,60]

In 1D superlattices, spherical Fe_3O_4 nanocrystals were self-assembled using molecular clusters complexed with oleylamine and $PbSO_4$, prepared by reacting lead chloride or lead oleate with excessive alkylammonium sulfate. Anisotropic 1D, highly ordered chain-type superlattices were formed with a single-nanocrystal width and a length of several micrometers (Figure 2g).^[20] In 3D superlattices, palladium nanocrystals passivated by different acid ligands self-assembled into superlattices with distinctly different geometric configurations.^[60] By comparing three different acid ligands, hexanoic acid, oleic acid, and 2-hexyldecanoic acid, the contribution of ligand entropy to crystallization was investigated. Results showed that nanocrystals capped with 2-hexyldecanoic acid were less stable than the other two acid ligands, so the superlattices dissolved back into dispersed nanocrystals more easily. As a result, the final size of superlattices with 2-hexyldecanoic acid was 30% smaller. In addition, the presence of carboxylic acid ligands was essential for the formation of Pd superlattices because nanocrystals could not assemble into superlattices when oleylamine completely replaced acid ligands. The ability of oleylamine to collapse superlattices was confirmed by the fact that the space between two nanocrystals increased with increasing the amount of oleylamine. The importance of capping ligands was also confirmed in multicomponent superlattices. For example, when a small amount of surfactant molecules such as oleic acid, tri- n -octylphosphine oxide (TOPO), and dodecylamine was added to colloidal solutions containing inorganic ($PbSe$, PbS , Fe_2O_3) and metallic (Au, Ag, Pd) nanocrystals, specific binary-component superlattices were formed as a result of modified surface charges.^[16] In another study, the structural analysis of AB_2 -type superlattices such as $MgZn_2$ and AlB_2 revealed specific growth orientations observed when different ligands were used.^[16]

In recent studies on metal–halide perovskite superlattices, capping ligands and their versatility were also demonstrated. As mentioned above, a similar strategy using $PbSO_4$ -oleate to construct 1D superlattices was also applied to the synthesis of metal–halide perovskite nanowires (Figure 4a).^[67] The overlayer of $PbSO_4$ -oleate serves as a template to induce linear alignment of individual building blocks (Figure 4b).^[68] Moreover, the $PbSO_4$ -oleate complex behaves like a polymer and inhibits anions from exchanging, providing a solution to the urgent problem of fast ion exchange in mixed halogen metal–halide perovskites (Figure 4c).^[69] In addition, capping with $PbSO_4$ -oleate enables nanocrystals to be linearly aligned when cast as

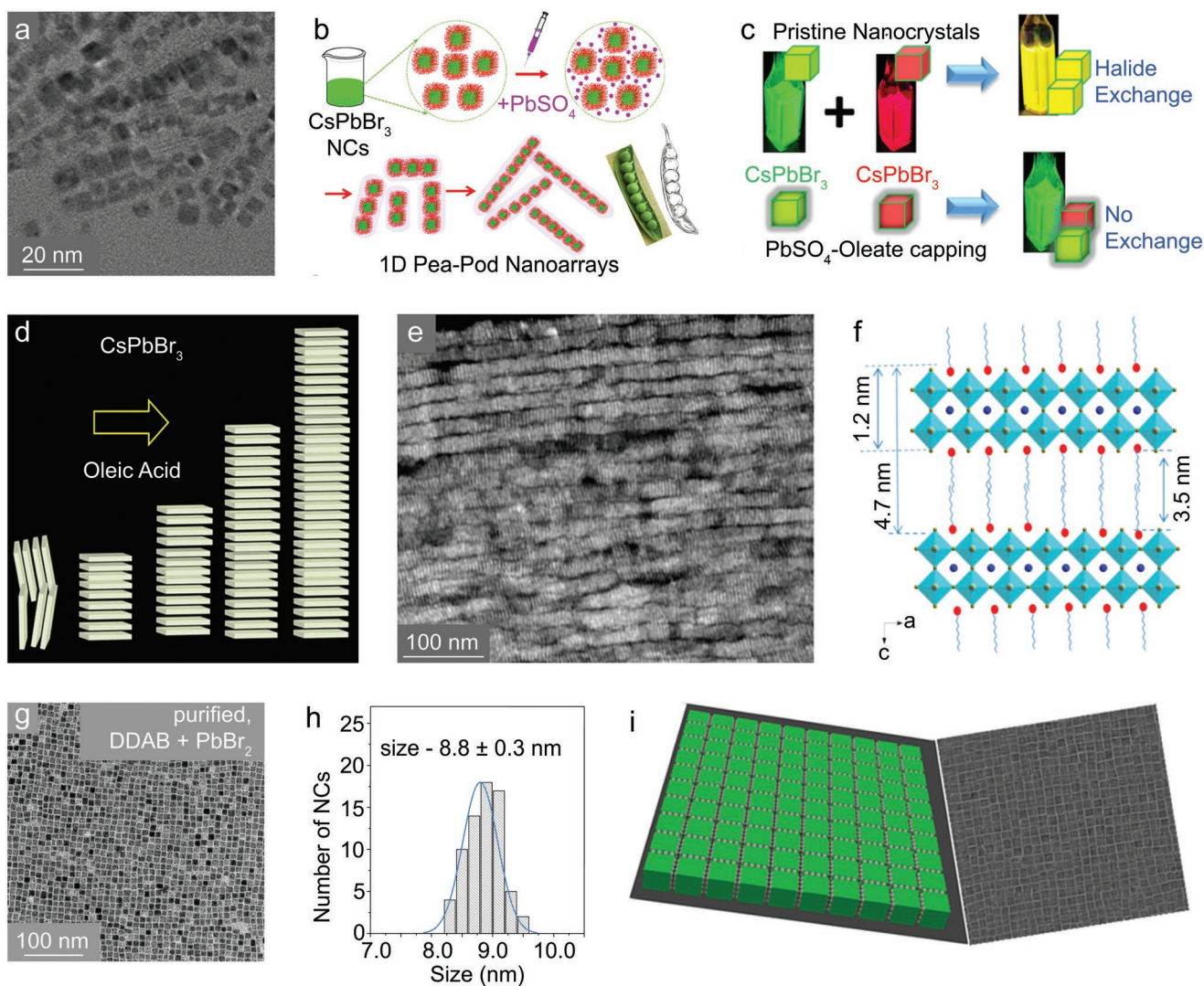


Figure 4. Various capping ligands for metal-halide perovskite superlattices. a) TEM imaging of 1D superlattices upon treatment with PbSO_4 -oleate. b) Schematic of the formation of 1D CsPbBr_3 peapod superlattices. c) Schematic showing that PbSO_4 -oleate inhibits the anion exchange of metal-halide perovskite nanocrystals. d) Schematic of oleic acid-induced assembly of CsPbBr_3 nanoplatelets into superlattices. e) HAADF-STEM imaging of nanoplatelet superlattices. f) Schematic of ligand interactions in nanoplatelet superlattices. g) TEM imaging of monodisperse CsPbBr_3 nanocrystals treated with DDAB ligand. h) The corresponding size histogram of the CsPbBr_3 nanocrystals shown in (g). i) TEM imaging of a thin film of ultrasmooth superlattices formed by short-chain SCN^- ligands. (a, c) Reproduced with permission.^[67] Copyright 2018, American Chemical Society. (b) Reproduced with permission.^[68] Copyright 2021, Royal Society of Chemistry. (d–f) Reproduced with permission.^[71] Copyright 2019, American Chemical Society. (g,h) Reproduced with permission.^[80] Copyright 2019, American Chemical Society. (i) Reproduced with permission.^[63] Copyright 2020, American Chemical Society.

films using an electrophoretic deposition technique, demonstrating their universality in various processes.^[70]

In 2D metal-halide perovskite superlattices of nanoplatelet type, the acid-amine equilibrium is of great importance for forming individual nanoplatelets and subsequent long-range assembly. Based on a systematic study, nanocrystal precursors containing more acid ligands than amine can self-assemble into nanoplatelets, followed by a further packing of long-range ordered superlattices (Figure 4d).^[71] These nanoplatelet-type superlattices were different from those of nanowire-type because their width was much larger (Figure 4e). Moreover, prolonging the reaction time without

any perturbation resulted in neater superlattices, indicating spontaneous assembly. Fine structure analysis showed that as the number of acid ligands increased, layered structures gradually emerged, which were quite similar to those in 2D layered hybrid perovskite materials (Figure 4f).^[72–76] The distance between layers was then identified as 2 times the ligand length, indicating a Ruddlesden-Popper configuration.^[77] In addition, the TOPO-mediated one-step approach proved effective for the formation of 2D nanoplatelets and superlattices using FAPbBr_3 (FA = formamidine).^[78] Given the bright deep-blue luminescence, better stability, and faster charge transport, these superlattices were used to fabricate a blue

light-emitting diode (LED), indicating that ligand-modulated self-assembly is possible for perovskites. In another study, high-quality ultrathin CsPbX₃ nanoplatelets and superlattice films were prepared by controlling the type and amount of capping ligands.^[79]

The importance of capping ligands in 3D metal–halide perovskite superlattices is mainly reflected in two aspects: size selection and shape retention. In fact, first-generation single-component metal–halide perovskite superlattices were achieved through rigorous size selection, which included several purification steps in order to obtain nanocrystals with less than 5% size deviations.^[47] The excellent size uniformity led to long-range ordering and high-quality superlattices with a small degree of spatial distortion. According to this guideline, several capping ligands have been developed to obtain dispersed nanocrystals with uniform sizes. For example, didodecylammonium bromide (DDAB) can passivate halide defects on nanocrystal surfaces by compensating for missing halide atoms, especially those nanocrystals that have been aged for a long period.^[80–83] In addition, these ligands prevent structural degradation and phase transition, thereby prolonging the life span of superlattices. More importantly, repaired nanocrystals feature a uniform size (size deviation: ≈3.4%), which facilitates the assembly of individual nanocrystals (Figure 4g,h). Another work found that thiocyanate (SCN[−]) ligands with short chain lengths are suitable for making nanocrystals with uniform sizes, resulting in thin film superlattices with a root-mean-square roughness of only 4 Å (Figure 4i).^[63] Compared with conventional 18-carbon oleyl chains, shorter SCN[−] ligands facilitate the arrangement of building blocks because the resulting nanocrystal assembly has a lower free energy. Furthermore, a sulfobetaine ligand, namely, 3-(*N,N*-dimethyloctadecylammonio)-propanesulfonate, can yield uniform nanocrystals, facilitating the formation of long-range ordered superlattices.^[84] Other two ligands with similar effects are α -halo ketone and didodecyltrimethylammonium sulfide.^[85,86]

A cuboid shape is another premise for growing superlattices of metal–halide perovskite nanocrystals. To prevent spherical growth during the assembly, a shorter capping ligand DDAB was used since the long hydrocarbon tails of typical ligands soften the cubic shape.^[47,87] Moreover, the deformation of DDAB allowed a very high packing density, which could be well predicted by OTM discussed in Section 2.1 (Figure 3b). In another work, metal–halide perovskite nanocrystals with pure shape and narrow size distribution were produced using secondary amines. Due to their inability to find the right steric conditions at nanocrystal surfaces, secondary amines were unable to form low-dimensional structures.^[88] High-quality superlattices with lateral dimensions up to 40 μm were obtained (Figure 6b).

Several ligands have a particular effect on the generation of metal–halide perovskite superlattices. For example, surface-bound 1-alkynyl acid was found to trigger a homocoupling reaction under ultraviolet (UV) irradiation, resulting in controlled assembly of metal–halide perovskite nanocrystals.^[89] By varying the carbon chain length of ligands, cuboidal and spindle-shaped superlattices were obtained. In another work, a gold–bromide complex was used to boost the assembly of metal–halide perovskite nanocrystals.^[90] Van der Waals interactions between carbon chains and electrostatic interactions

between Au–Br complexes and surfactants were found to be the driving forces.

2.3. Synthetic Methods

In principle, ordered superlattices are self-assembled from colloidal nanocrystals by evaporation, destabilization, or gravitational sedimentation of a concentrated precursor solution.^[13,91–94] A typical method is to evaporate the solvent in a vacuum environment at a moderate temperature, which causes nanocrystals inside the solution to cluster together at the late stages of solvent drying.^[95] Nanocrystal cores are protected from disintegration by capping ligands that balance microscopic attraction and repulsion forces. Polar or nonpolar solvents are often used to change the polarity of the solution.^[96] As with the reversed micelle method, the driving force is derived from the difference in affinity between nanocrystals in two solvents. In the case of gravitational sedimentation, superlattices usually grow in solutions containing nanocrystals with a diameter approaching 1 μm , or nanocrystals with heavy metal atoms packed densely.

For metal–halide perovskite superlattices, the evaporation method is the most common technique. Typically, several droplets containing purified nanocrystals in a nonpolar solution (e.g., a total of 10 μL in toluene) are spread on a substrate and then slowly evaporated (Figure 5a,b). Temperature and pressure are key parameters to obtain high-quality superlattices. In a vibration-free environment, moderate temperatures and vacuum (e.g., room temperature and 0.45 atm pressure) are helpful in obtaining large-area superlattices within a short period of time.^[49] At low temperatures and ambient pressure, metal–halide perovskite superlattices can also be formed after prolonged aging.^[97–99] It is evident that the substrate selected for supporting the solution has an effect on the optical properties of resultant superlattices. For example, superlattices grown on dielectric Si₃N₄ membranes display better collective superfluorescence than those grown on carbon-coated copper transmission electron microscopy (TEM) grids.^[100] This is because superlattices and conductive carbon films interact strongly, accelerating coherent dipole dephasing and weakening collective emission.

The destabilization approach has been used in several research projects. By controlling the polarity of solvents, 1D superlattices can be formed in hexane, whereas 2D superlattices can be assembled in a more polar solvent such as ethyl acetate (Figure 5c).^[93] Hydrophobic forces between ligands and nonpolar solvent molecules and van der Waals forces between alkyl ligands in a nonpolar solvent are responsible for the growth of 1D superlattices, while minimization of repulsive forces between the solvent and ligands causes proximal nanocrystals to form 2D superlattices. As a modified gravity sedimentation method, single-step centrifugal casting has proven effective in preparing perovskite films with dense and homogeneous morphology (Figure 5d).^[101] Notably, superlattice films with different halide compositions can be assembled using this method (Figure 5e).

Since evaporation is the most practical and efficient means to manufacture metal–halide perovskite superlattices to date, the

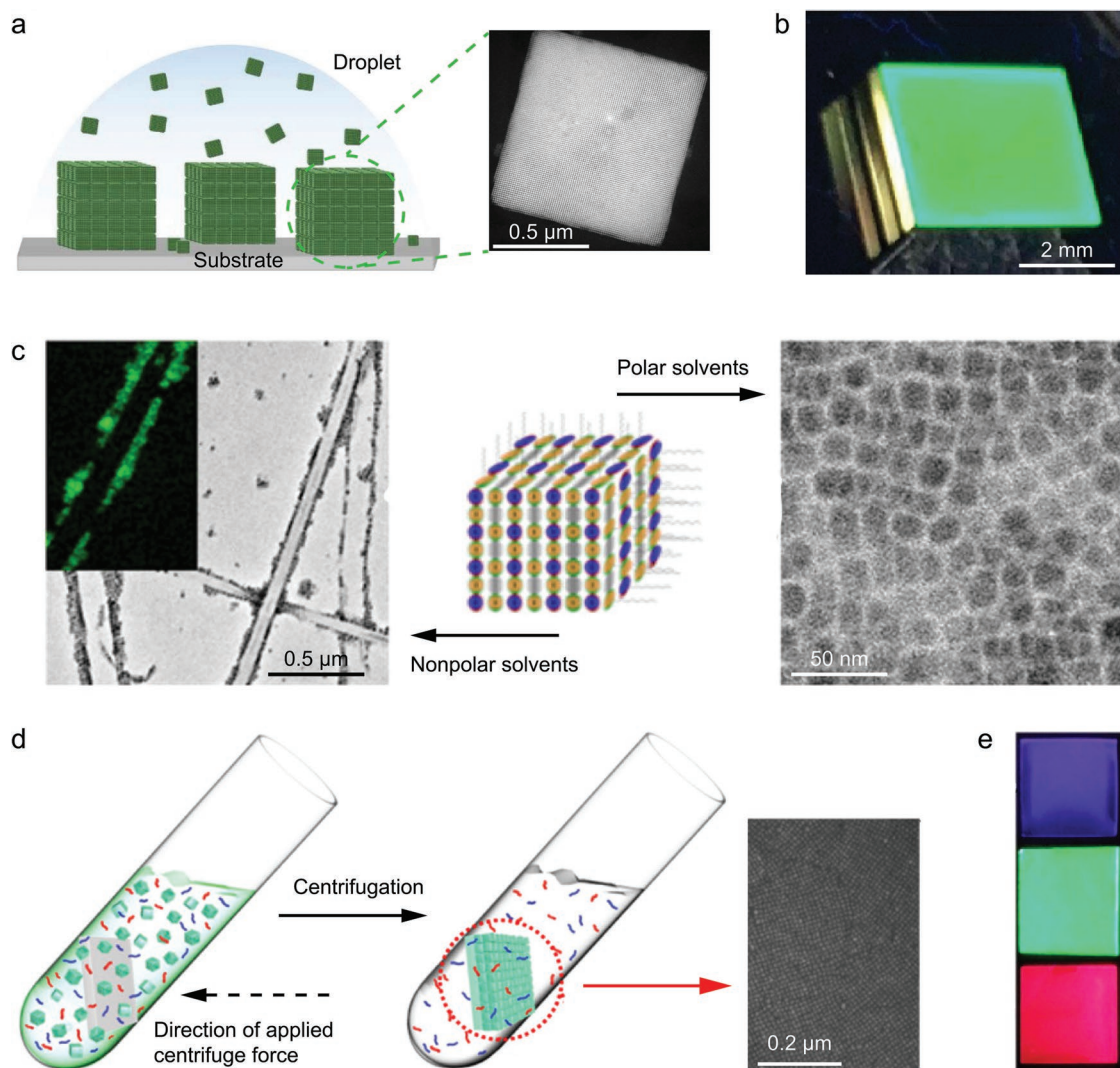


Figure 5. Synthetic methods for perovskite nanocrystal superlattices. a) Schematic illustration of the assembly process (left) and the resulting superlattice (right). b) Photograph of a layer of CsPbBr₃ superlattice film under UV light. c) TEM image of 1D superlattice made of CsPbBr₃ nanocrystals (left) and 2D assemblies (right). Inset is the composition mapping. d) Schematics of a centrifugal casting process used to fabricate CsPbBr₃ superlattice films (left) and TEM image of the corresponding superlattice (right). e) Superlattice films with different compositions under UV excitation. (a, b) Reproduced with permission.^[47] Copyright 2018, Springer Nature. (c) Reproduced with permission.^[93] Copyright 2017, American Chemical Society. (d, e) Reproduced with permission.^[10] Copyright 2015, American Chemical Society.

discussion below is primarily based on evaporation-prepared samples, unless otherwise specified.

2.4. Structure Identification

The synthesis of metal–halide perovskite superlattices requires the formation of highly ordered structures during self-assembly. As a result, structure identification is critical. Confirmatory methods include optical microscopy, electron microscopy, and synchrotron-based X-ray scattering techniques, depending on the size and structural differences between superlattices and dispersed nanocrystals.^[13,47,49,102]

Because metal–halide perovskite superlattices are generally several micrometers wide, a simple optical microscope can be used to view their shapes (Figure 6a). This is exactly the original

method used to observe the first CdSe nanocrystal superlattices (Figure 2a).^[13] Metal–halide perovskite superlattices can be visualized using confocal microscopy when stimulated by UV or blue light. For example, confocal microscopy can be used to produce green photoluminescence images of CsPbBr₃ superlattices under 488 nm excitation (Figure 6b).^[88] On a micrometer length scale, these superlattices display spatially uniform photoluminescence, with no evidence of nanocrystal aggregates.

Scanning electron microscopy (SEM) and TEM are commonly utilized to provide structural information in real space.^[47,49] In SEM, primary electrons interact with samples and generate secondary electrons. Signals carried by these secondary electrons are translated into SEM images of sample morphology. SEM can only record large-area superlattices with several tens of micrometers of width. For high-magnification TEM, signals can be collected and analyzed from electrons

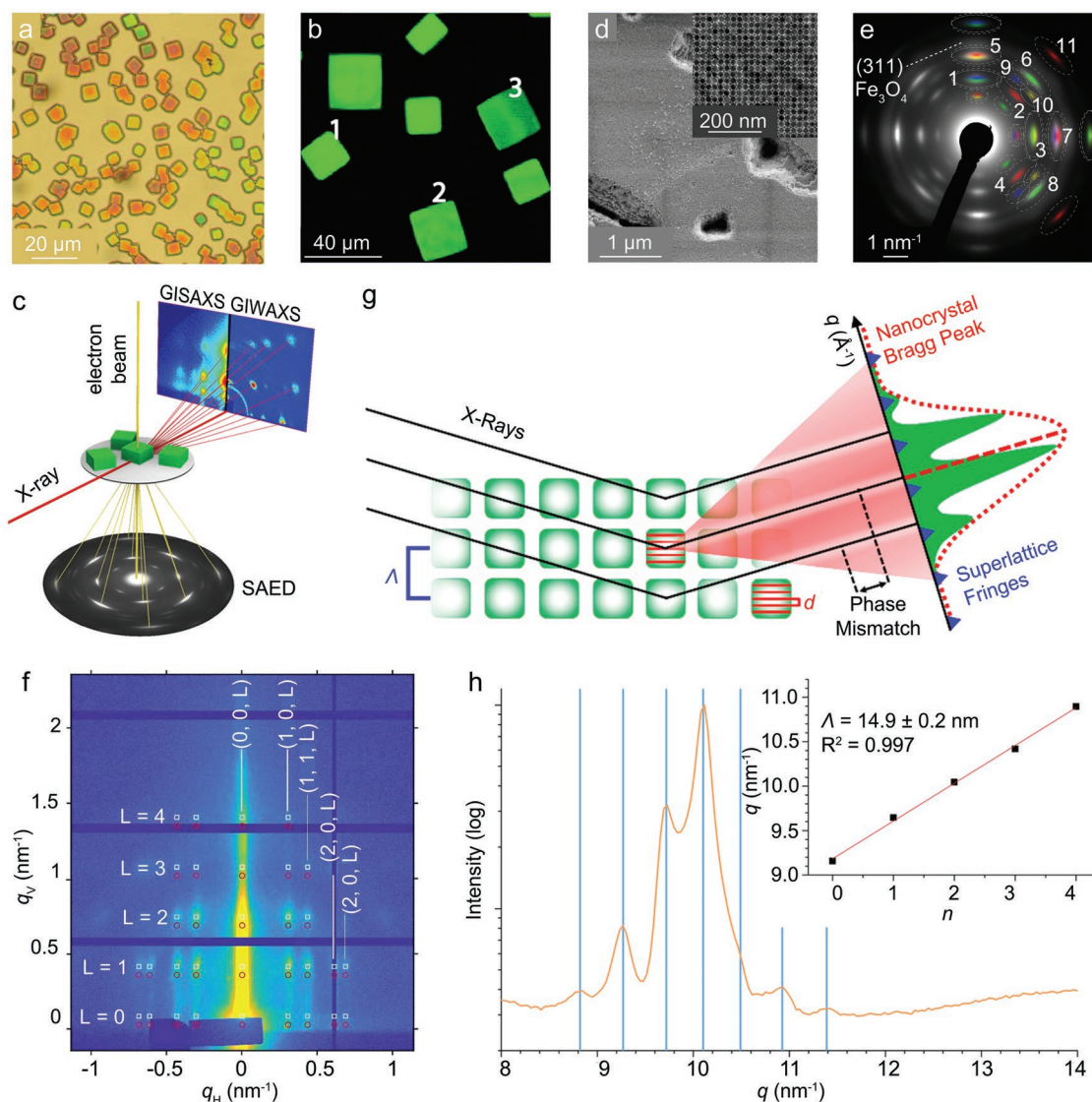


Figure 6. Methods for identifying the structure of ordered superlattices. a) Photograph of CsPbBr₃ superlattices. b) Confocal microscopy image of CsPbBr₃ superlattices. c) Working principles of electron microscopy, GISAXS, and GIWAXS techniques. d) Low-magnification SEM image of a Fe₃O₄-CsPbBr₃ superlattice domain. e) SAED pattern of the superlattice in (d). f) GISAXS scattering image of the superlattice in (d). g) X-ray scattering method for illustrating nanocrystal Bragg peaks and superlattice fringes. h) XRD peak splitting within a small-angle region in FASnI₃ superlattices. (a) Reproduced with permission.^[47] Copyright 2018, Springer Nature. (b) Reproduced with permission.^[88] Copyright 2018, American Chemical Society. (c,g) Reproduced with permission.^[102] Copyright 2021, American Chemical Society. (d-f) Reproduced with permission.^[49] Copyright 2021, Springer Nature. (h) Reproduced with permission.^[105] Copyright 2021, Springer Nature.

penetrating thin specimens of no more than a few tens of nanometers in thickness. In a typical measurement, accelerated electron beams are generated to penetrate samples (Figure 6c). During collisions with atoms, electrons are scattered in multiple directions, creating 2D or 3D images. Since scattering angle is proportional to sample density and thickness, sharp images can be obtained. Based on TEM results, reciprocal space images from selected area electron diffraction (SAED) and fast Fourier transform modes enable precise nanoscale and atomic-scale analysis of periodic lattices (Figure 6c,d). The SAED pattern of a multicomponent metal-halide perovskite superlattice can reveal colored diffraction spots associated with different lattice planes of CsPbBr₃ (Figure 6e).^[49] A variety of advanced

electron microscopy techniques have been applied to acquire high-quality images of superlattices, including high-resolution transmission electron microscopy (HRTEM), high-angle annular dark field transmission electron microscopy (HAADF-TEM), and scanning transmission electron microscopy (STEM).

Synchrotron-based grazing-incidence small-angle X-ray scattering (GISAXS) and grazing-incidence wide-angle X-ray scattering (GIWAXS) techniques are contemporary approaches for superlattice characterization. X-rays have deep penetration capability, which allows structure identification in almost all kinds of superlattices, regardless of material type, packing density, assembly orientation, and crystal thickness. In these two measurement methods, X-rays propagate almost parallel to the

sample surface (Figure 6c).^[102] After excitation of the samples, scattered signals are collected and analyzed. It should be noted that there is no significant difference between GISAXS and GIWAXS, since the distance between the detector and the samples decides the ultimate diffraction regions, i.e., the farther apart they are, the smaller the angle obtained. The GISAXS technique focuses on signals within small angles, whereas the GIWAXS technique exhibits a much wider scattering angle and more diffraction spots with periodic features.

When X-rays strike superlattices, they are first diffracted at the atomic planes of individual nanocrystals, which act as diffraction gratings. Each nanocrystal produces a diffraction profile with an intrinsic size broadening that forms a broad peak with weak side ripples (Figure 6g).^[102] Thus, due to the periodic arrangement in superlattices, a series of the aforementioned patterns can be obtained within certain detection angle ranges.^[103] A GISAXS scattering image of a multicomponent superlattice made of CsPbBr₃ and Fe₃O₄ nanocrystals shows nearly perfect periodic patterns, indicating their high crystalline quality (Figure 6f).^[49] Because GISAXS and GIWAXS tests are resource demanding, high-resolution wide-angle X-ray diffraction may be more practical for assessing superlattice structures.^[104] Peak splitting in the small-angle regime can be considered an indication of ordered structures (Figure 6h).^[105]

The multilayer diffraction method is another powerful tool for evaluating the structures of perovskite nanocrystal superlattices in terms of particle size, interparticle spacing, and the corresponding fluctuations.^[79,102] In the case of large-area Cs–Pb–I–Cl Ruddlesden–Popper nanoplatelet superlattices ($\approx 50 \mu\text{m}$), the nanoplatelet thickness, interparticle spacing, degree of stacking disorder, and surface coverage rate were precisely determined by comparing multilayer diffraction fitting data with documented bulk parameters.^[79] Traces of CsPbCl₃ impurities were also identified. The major advantage of this technique is that only a laboratory-grade diffractometer and an open-source fitting algorithm are required for data analysis.

3. Optical Features of Metal–Halide Perovskite Superlattices

The assembly of metal–halide perovskite nanocrystals into superlattices is invariably accompanied by unique optical features, including superfluorescence, amplified spontaneous emission (ASE), and spectral redshift.^[47,49,81,82,84,106–112] Superfluorescence has been rarely observed, except in π -conjugated poly(phenylene vinylene) derivatives and O₂[−] centers in KCl single crystals, both of which were reported almost 50 years ago.^[113,114] Another optical phenomenon, known as superradiance that resembles superfluorescence, has long perplexed researchers.^[115] Before analyzing the optical features of metal–halide perovskite superlattices, it is vital to clearly distinguish between them.

In 1954, Dicke predicted the coherent emission of a two-energy level system without a laser cavity, which was often considered an optical gain structure for ASE generation.^[116] In the following years, researchers discovered two different pathways of coherent emission, which were named Dicke superradiance and superfluorescence.^[48] A quasi-four-level energy diagram is

used here to provide actual details on these two distinct optical features (Figure 7). ASE is also included for a more holistic understanding.^[117] In the case of superradiance, an external high-energy laser coherently pumps electrons in the ground state E₁ to a stable excited state E₃, producing a large number of excitons. These excitons behave like a macroscopic dipole with identical phases, i.e., coherent. After releasing excitation energy, they undergo radiative transitions from E₃ to subground state E₂, generating coherent superradiance (Figure 7a). During the photophysical process, excited electrons and holes form an array of dipoles with the same phase within an extremely short time τ_p and exhibit a “memory” behavior, followed by super-radiant emission. As such, superradiance can be defined as a transient process in which excitation source, excitonic dipoles, and emission are all coherent.

In contrast to superradiance, superfluorescence was always posterior to conventional fluorescence (Figure 7b).^[47,49,113] Electrons jump from E₁ to the excited state E₄ under laser excitation. Since E₄ has a short lifetime, electrons thermally relax to the low-lying excited state E₃, which is assisted by phonons. Some of the electrons or excitons with random dipole directions spontaneously return to the ground state E₁ and emit fluorescence incoherently as usual. Fluorescence can induce a macroscopic dipole within a short period of time τ_D , resulting in identical dipole phases for the remaining excitons, followed by a coherent superfluorescence emission with a wavelength equivalent to the energy gap between E₃ and E₂. In this respect, superfluorescence is a concomitant process that occurs shortly after conventional spontaneous emission.

Both coherent and incoherent excitation sources work for ASE. Laser excitation is used to align ASE with superradiance and superfluorescence (Figure 7c). As with superfluorescence, laser stimulation excites electrons to E₄ before phonon relaxation to E₃. Notably, excitons at the E₃ state have random dipole vectors. In an ASE system, fluorescence with various phases can be enhanced by stimulated emission, but a specific phase’s maximal gain gradually dominates, followed by electrons dropping from E₃ to E₂.^[118] Since E₂ has a much shorter lifetime than E₃, electrons are rapidly released to E₁, causing population inversion between E₃ and E₂ and eventually a cooperative output. Since laser generation requires a pump source, gain medium, and resonant cavity, ASE can be modulated by introducing resonant cavities such as the whispering gallery mode and the Fabry–Perot mode.^[119,120] As such, ASE can be understood as a mirrorless laser.

Since superradiance, superfluorescence, and ASE all behave as stimulated emission, their occurrence is largely determined by population inversion. In particular, the optical properties of superradiance and superfluorescence are quite similar, including sharp emission peaks, pump-power-dependent exponential increases in output intensity, reduced decay times, and directionality and polarization of emission beams, making accurate identification difficult.^[117] Below are several suggestions on how to differentiate these three optical phenomena. In terms of time domain emissions, superradiance and superfluorescence have coherent characteristics such as interference effects, quantum beats, and Burnham–Chiao ringing, but ASE does not possess any of these properties. Moreover, the delay time τ_D is a unique feature of superfluorescence. For both

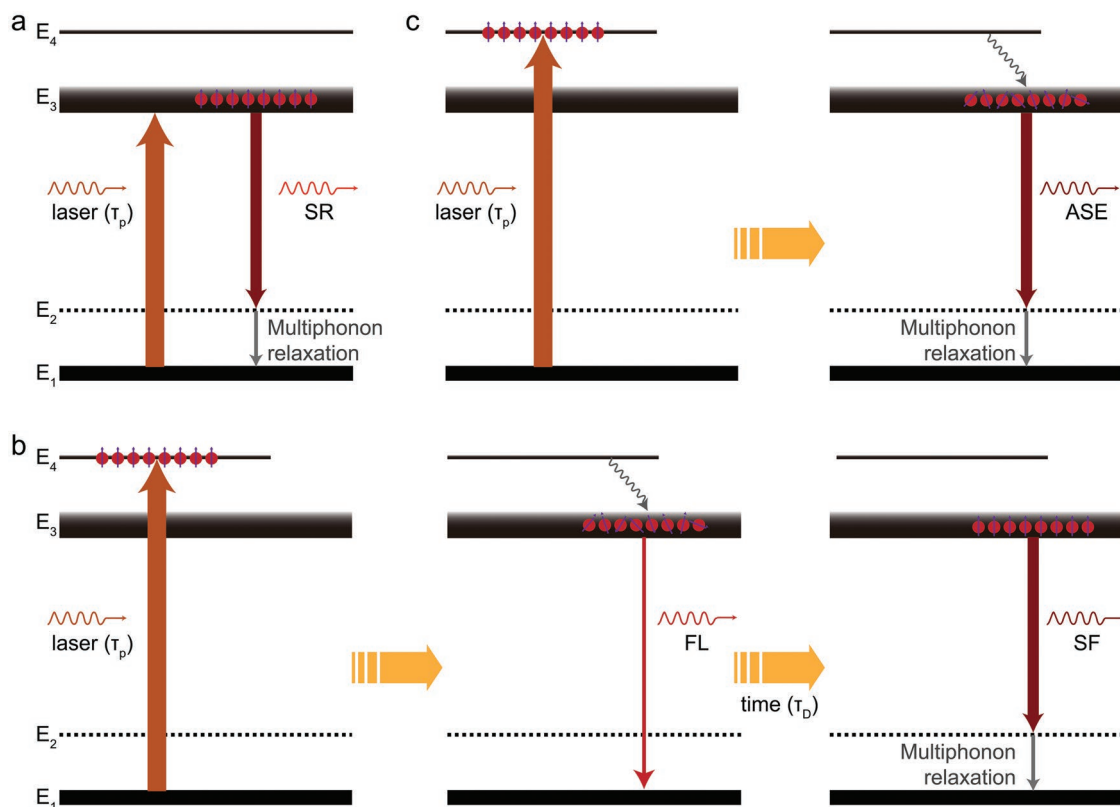


Figure 7. Quasi-four-level diagrams depicting three optical transitions. a) Superradiance (SR), b) superfluorescence (SF), and c) amplified spontaneous emission (ASE). E₁: ground state; E₂: subground state at which electrons return to the ground state through multiphonon-mediated nonradiative decay; E₃: stable excited state with a long lifetime; E₄: unstable excited state with a short lifetime. Red circles with purple arrows: dipoles and their phase vectors. τ_p stands for the lifetime of the pumping laser. τ_D is the time interval for the formation of a macrodipole after fluorescence.

superradiance and superfluorescence, well-defined exponents can be obtained by fitting emission intensity versus pump power, while exponents for ASE can be any number. Last but not the least, an empirical index T_2 can be used to distinguish ASE from superradiance and superfluorescence by comparing T_2 to τ_p. For instance, T_2 in ASE is often significantly shorter than τ_p, which is discussed in Section 3.2.^[121]

3.1. Superfluorescence

In a system with spontaneous emission, the fluorescence comes from independent excited atoms, each unit interacts neither with others nor with the radiation field.^[122] Therefore, the maximum intensity I_{\max} of isotropic fluorescence is proportional to the number of excited atoms. Moreover, the corresponding decay rate obeys an exponential law with a characteristic time τ_n equal to the reciprocal of the radiative decay rate of the individual exciton.

In contrast to isotropic spontaneous emission with unpolarized excitons, superfluorescence is highly anisotropic, corresponding to the sample geometry. In a typical superfluorescence involving coherent excitons (number N), its intensity follows the rule $I_{\max} \propto N^2$, it requires a short buildup period τ_D ∝ (lg N)/ N , and the resulting collective decay time τ_R ∝ τ_n/ N is much shorter than conventional fluorescence (Figure 8a).^[122]

As for the experiment, several principles must be satisfied for the observation of superfluorescence. First and foremost, interactions between dipoles and the light field are necessary. Furthermore, the mean interatomic distance between nanocrystal units must be much smaller than their emission wavelength. In addition, other types of interactions such as collisions and thermal noise should be minimized to prevent exciton wavefunction dephasing.^[121] Once the atomic system becomes dense, large, and cold enough, several initially independent dipoles will resonate in identical phases to form a macroscopic dipole. As a result, energy is coherently released, leading to superfluorescence. It should be noted that the energy of the macroscopic exciton is not released by a single pulse but in the form of a series of pulses of diminishing size, which is defined as Burnham–Chiao ringing, first detected by Burnham and Chiao in 1969.^[123]

It was discovered in 1973 that HF gas exhibits superfluorescence at room temperature.^[115] Almost 50 years later, this intriguing optical feature was detected in metal–halide perovskite superlattices.^[47] These superlattices were prepared by the solvent evaporation method, in which dispersed CsPbBr₃ nanocrystals self-assembled into an elongated, highly ordered configuration (Figure 6a,b). Comparing individual nanocrystals with their superlattices, it is apparent that fluorescence has a common exponential damping time τ_{FL}, while superfluorescence has a short collective decay period τ_{SF} (Figure 8b).^[47,121]

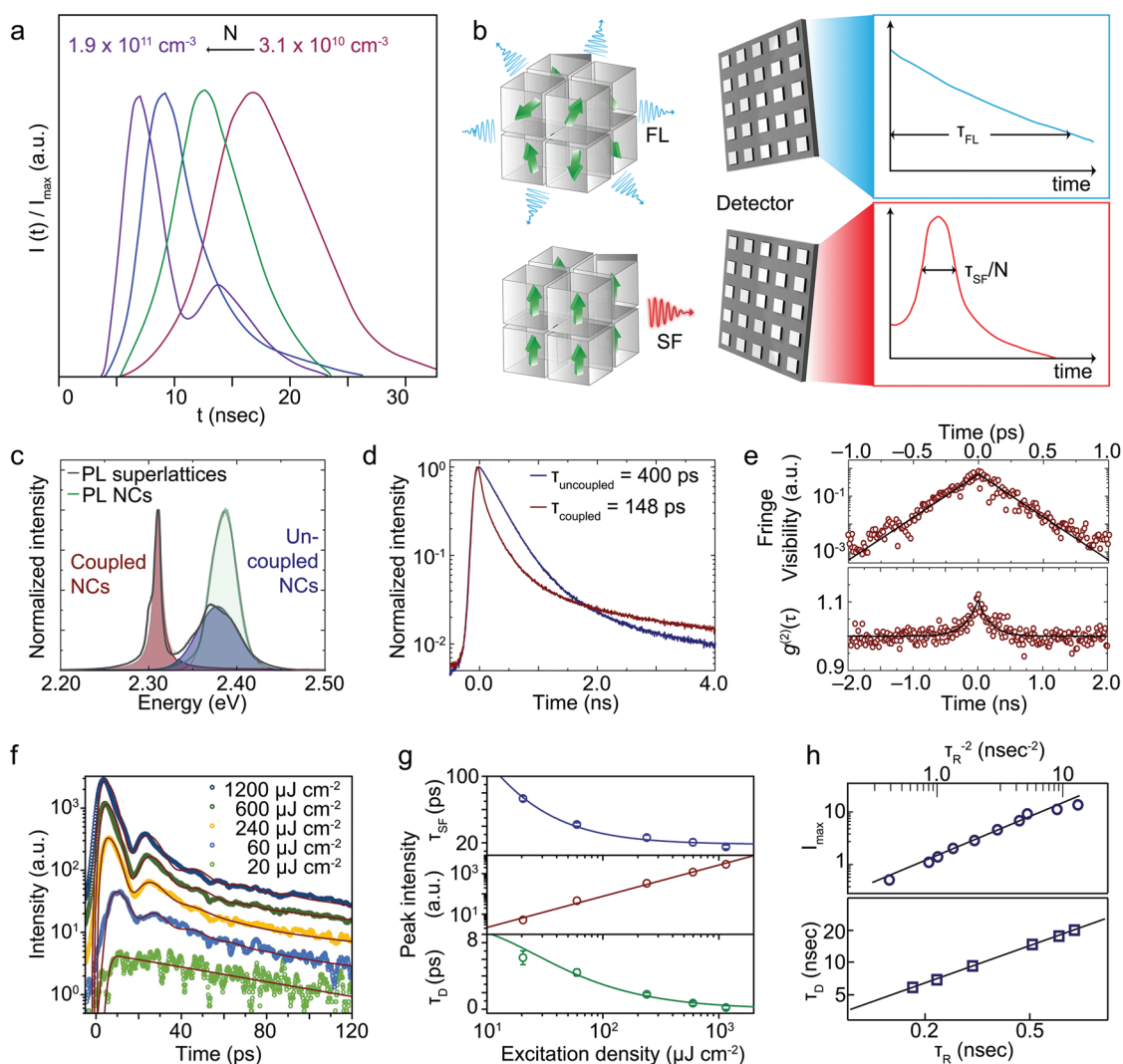


Figure 8. Unique optical characteristics of superfluorescence in metal-halide perovskite superlattices. a) Relationship between the number of coherently excited atoms N and the superfluorescence decay time. b) Schematic of fluorescence and superfluorescence. c) Photoluminescence spectra of nanocrystals and superlattices. d) Time-resolved photoluminescence decay of two emission peaks in (c). e) First-order (top) and second-order (bottom) coherence behavior of superlattices. f) Time-resolved emission intensity trace under different excitation powers. g) Superfluorescence decay τ_{SF} (top), superfluorescence emission intensity (middle), and collective delay time τ_D (bottom) as a function of laser power. h) Optical features of superfluorescence from HF gas. (a,h) Reproduced with permission.^[122] Copyright 1996, IOP Publishing. (b–g) Reproduced with permission.^[47] Copyright 2018, Springer Nature.

Two peaks appear in the photoluminescence spectrum of superlattices, one with higher energy due to uncoupled nanocrystals fluorescence and another with lower energy due to superfluorescence (Figure 8c). The coherent release of excitons contributes to the much faster emission decay (Figure 8d). A Michelson interferometer was used to measure phase coherence in superlattices, and it was found to be 3.5 times longer than in nanocrystals, indicating coherent processes (Figure 8e). Second-order analysis of photon arrival time confirmed pronounced photon bunching, indicating a time delay between fluorescence and superfluorescence (Figure 8e). Moreover, Burnham–Chiao ringing was observed in superlattices by streak cameras, and the ringing became more evident with increasing laser power (Figure 8f). At higher laser power, superfluorescence decay time τ_{SF} , intensity, and collective

delay time τ_D all matched those of superfluorescence observed in HF gas (Figure 8g,h), in that I_{max} was linear to τ_R^{-2} and τ_D was linear to τ_R , confirming that superfluorescence was emitted in metal-halide perovskite nanocrystal superlattices.^[121] In 2021, superfluorescence was observed in ABO₃-type superlattices comprising NaGdF₄ and CsPbBr₃ nanocrystals, where the former occupied A-site and the latter occupied other sites.^[49] By precisely controlling the size of NaGdF₄ nanocrystals, the distance between two compositions could be regulated to promote superfluorescence.

The detection of superfluorescence is only possible at cryogenic temperatures around 6 K due to thermal dephasing. This explains that the measured radiative decay rate is six orders of magnitude smaller than theoretically expected.^[124] This quenching behavior severely hinders the practical

applications of superfluorescence. A promising strategy to address this issue is the introduction of polarons, as demonstrated in MAPbI₃ (MA: methylamine) thin films at 78 K.^[125] By adding organic molecules such as phenethylammonium (PEA), it is possible to construct quasi-2D PEA:CsPbBr₃ thin films that are resistant to thermal quenching and superfluorescence can be detected at temperatures above 300 K.^[126] These anomalous phenomena are attributed to strongly bound exciton polarons in hybrid perovskites, which can stabilize the coherence process and lead to more macroscopic quantum phase transitions.

In superlattices of binary components, a slight change in the size and mixing fraction of spherical Fe₃O₄ and cubic CsPbBr₃ nanocrystals leads to a crystalline transition from the NaCl type to the perovskite type. Notably, enhanced superfluorescence was observed in the latter, indicating strengthened coherent dipole coupling.^[49]

3.2. Amplified Spontaneous Emission

Einstein predicted ASE in his seminal paper on radiation a century ago.^[127] This phenomenon is based on symmetric absorption and induced emission, and it can be seen in any optical system with gain mode. ASE is described as a sequence of optical transitions in gain media, in which all types of spontaneous emission within gain can be amplified by stimulated emission, and the emission with the maximum enhancement gradually dominates, eventually resulting in cooperative output.^[128] In terms of exciton behavior, ASE is similar to superfluorescence, with the main difference being that the dipole

phase of excitons in the emitting state is random for the former but accordant for the latter (Figure 7c). A dephasing time T_D is used to differentiate them, which is the synergistic result of collective decay time and buildup time.^[129]

Given that the dipole dephasing rate is proportional to the third power of temperature, a certain optical system exhibits different phenomena as the temperature fluctuates.^[122] For example, with increasing temperature, the proportion of superfluorescence gradually decreases, while ASE increases until it dominates (Figure 9a). The emitted pulse broadens monotonically, signaling the gradual weakening of superfluorescence. In such processes, there is a watershed dividing the dephasing rate into two parts, a fast-dephasing regime for superfluorescence and a slow dephasing region for ASE (Figure 9b). Temperature has a significant influence on superfluorescence intensity because dipole alignment is highly sensitive to temperature. With a temperature increase of only 15 K, the maximum emission intensity decreased over six orders of magnitude, suggesting a transition from superfluorescence to ASE (Figure 9c).

A schematic depicting all optical features of ASE is shown in Figure 9d for clarity.^[117] As ASE is a noncoherent emission, the emitted photons have no direction selectivity. Considering that a macroscopic dipole alignment can be achieved in given microcavities, as seen for dominant radiation along the direction toward the right in cylinder-type gain medium, the geometry of a certain optical system usually has a substantial impact on ASE. This output can be regarded as a directional beam that falls between a truly coherent laser oscillator and a completely incoherent fluorescence. In this regard, ASE is a prerequisite for generating laser, which is why ASE was formerly referred

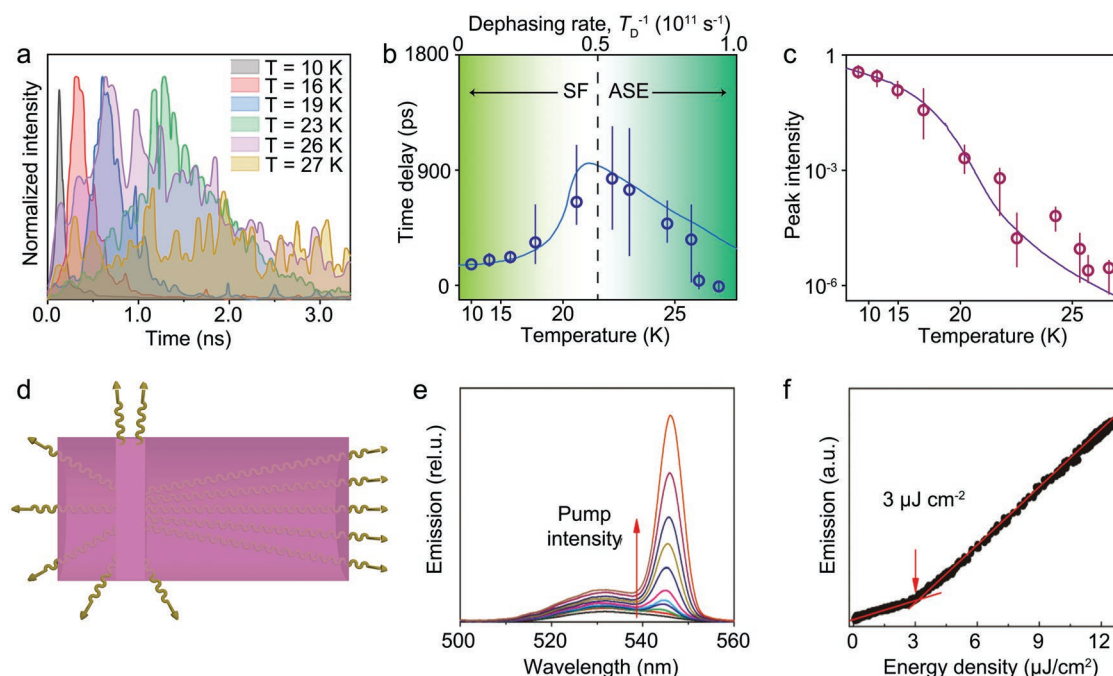


Figure 9. Amplified spontaneous emission in metal-halide perovskite superlattices. a–c) Temperature-dependent variations in photoluminescence spectrum, dephasing rate, and peak intensity, respectively. d) Schematic of ASE in a cylinder gain model. e) Pump-power-dependent photoluminescence spectra of MAPbBr₃ superlattices. f) Extracted emission intensity versus energy density. (a–c) Reproduced with permission.^[122] Copyright 1996, IOP Publishing. (e,f) Reproduced with permission.^[130] Copyright 2016, The Royal Society of Chemistry.

to as a mirrorless laser. The entire process can be summarized as follows: upon excitation with a light source, the number of emitted photons is increased by gain media, and a microcavity then modulates unaligned photons toward a specific orientation, producing the laser beam.

Numerous studies have been conducted on ASE from metal-halide perovskite materials. ASE can be achieved with ease if the pump power is sufficient. A large pumping density results in an increased ASE intensity, and the transition from spontaneous emission to ASE is known as the threshold.^[128] Successful observation of a sharp emission peak on the photoluminescence spectrum indicates the generation of ASE.^[130] For example, MAPbBr₃ (MA = methylamine) superlattices show an ASE peak with a bandwidth of 7–9 nm compared to 20 nm at the outset (Figure 9e). The biexcitonic nature of the optical gain is responsible for the redshift of ASE from the photoluminescence maximum. The total emission intensity extracted from this material shows an inflection point corresponding to the threshold of ASE (Figure 9f). The intensity versus pump density after the threshold shows a superlinear relationship until exciton saturation. The threshold for MAPbBr₃ superlattices was 3 μJ cm⁻², 3 times lower than that of randomly distributed building blocks. A reduction in biexciton binding energy and an increase in carrier cooling rates in superlattices are believed to be responsible for this lower threshold.^[131] Another study showed that upon 800 nm excitation, ASE appears in 2D photonic CsPbBr₃ supercrystals at a pump fluence of 10.9 mJ cm⁻², indicating facilitated light coupling between individual nanocrystals.^[132]

It should be noted that stimulated superfluorescence amplified by modulation of microcavities can also be obtained, which shows quite similar spectral features to ASE. For example, the

peak of microcavity-enhanced superfluorescence in CsPbBr₃ superlattices appeared narrower and more intense when the pumping power exceeded 40 μJ cm⁻².^[107] The geometry selection characteristic of ASE can be used to distinguish lasers from superfluorescence and ASE modes. After changing microcavity geometries, stimulated superfluorescence amplification causes the lasing beam to change shape or wavelength.^[107,108] Additionally, superfluorescence lasing has a higher threshold than ASE lasing.^[110]

3.3. Quantum Wells and Spectral Redshift

In 2D layered perovskite thin films, the formation of quantum wells and subsequent occurrence of spectral redshift are frequently caused by the accumulation of dispersed nanocrystals into superlattices.^[133–135] When it comes to the quantum confinement effect, metal-halide perovskite nanocrystals smaller than their Bohr radii are characterized by a larger bandgap between the valence band and conduction band edges, resulting in a blueshift in the emission peak.^[22] On the contrary, redshift appears to be a reversal of quantum confinement, in which individual nanocrystals in superlattices interact strongly with one another, generating a smaller bandgap (Figure 10a). The underlying rationale for bandgap narrowing is that enhanced electronic wavefunction interactions between neighboring nanocrystals within superlattices lead to multiple minibands.^[3] Therefore, optical transitions involving these minibands usually feature lower energies, corresponding to the experimentally observed spectral redshift. Quantum wells are typically formed in 2D layered perovskites, mainly due to the strong dielectric screening of A-site organic

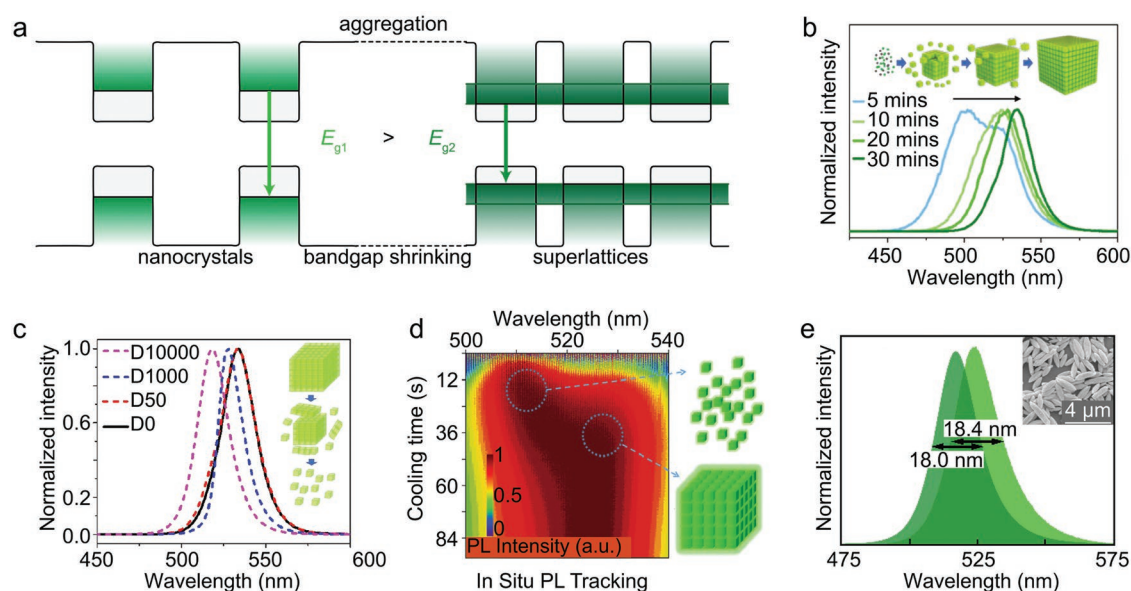


Figure 10. Quantum wells and spectral redshift in CsPbBr₃ nanocrystal superlattices. a) Schematic of quantum wells in superlattices. Reversible spectral redshift in b) superlattice formation from dispersed nanocrystals and c) superlattice disassembly to dispersed nanocrystals. d) In situ observation of spectral redshift. e) Photoluminescence peaks of dispersed nanocrystals (left) and spindly superlattices (right). Inset is the corresponding SEM image of superlattices. (b,c) Reproduced with permission.^[30] Copyright 2018, Wiley-VCH. (d) Reproduced with permission.^[112] Copyright 2020, American Chemical Society. (e) Reproduced with permission.^[89] Copyright 2020, Wiley-VCH.

molecules with poorer electroconductivity than inorganic octahedra. This forces electrons to be effectively localized around inorganic octahedra and recombine with holes, resulting in photon emission.^[136]

A close relationship exists between the photoluminescence peak of metal–halide perovskite superlattices and their size. For example, by prolonging the aging process for self-assembly, larger superlattices are formed, and the redshift is more evident as elementary building blocks interact more strongly (Figure 10b).^[30] An upper limit for redshift exists because the superlattice’s size is finite due to the equilibrium between aggregation and disassembly. Interestingly, the spectrum can be recovered by dissolving superlattices into their original nanocrystal forms. For instance, a 10 000-fold dilution of CsPbBr₃ superlattices shifts its photoluminescence from 530 to 515 nm (Figure 10c).^[30] Moreover, in situ ultrafast spectroscopic techniques that detect the spectral redshift in the self-assembly process can be used to investigate the growth dynamics and kinetics of superlattices (Figure 10d).^[112]

Spectral redshift is not only a characteristic of superlattices with cuboidal shapes, but also a universal property of all superlattices. For example, the carbon chain length of organic ligands can be varied to achieve a 20 nm redshift in spindly CsPbBr₃ superlattices with different aspect ratios (Figure 10e).^[89] The shape of emission spectrum of such superlattices is almost the same as that of diluted nanocrystals, except for a negligible difference in half-width.

4. Applications of Metal–Halide Perovskite Nanocrystal Superlattices

The unique optical properties of metal–halide perovskite superlattices are challenging to characterize because cryogenic temperatures, advanced instrumentation, and precise growth parameters are required. We discuss preliminary applications in this section, including their use as terahertz quantum containers and as standard green luminescent layers in LEDs.^[30,107]

4.1. Terahertz Quantum Containers

Metal–halide perovskite nanocrystal superlattices with microcavity enable amplified stimulated superfluorescence lasers with wavelength selectivity without affecting their coherent phase.^[107–110] An interesting example involves a CsPbBr₃ superlattice microcavity acting as a dual-state terahertz (THz) quantum container (Figure 11a).^[107] The existence of excitonic quantum ensembles represents “filled” states, whereas the absence of cooperative dipoles indicates “void” states. Traditionally, containers are filled upon optical pumping, but become void after a slow nonradiative decay. However, radiative relaxation can empty the superlattice quantum container, and more importantly, residual carriers can be rapidly dephased to form a “void” quantum state. It is possible to modulate THz quantum containers directly and expeditiously between two states within a significantly shorter control period, as short as 10 ps

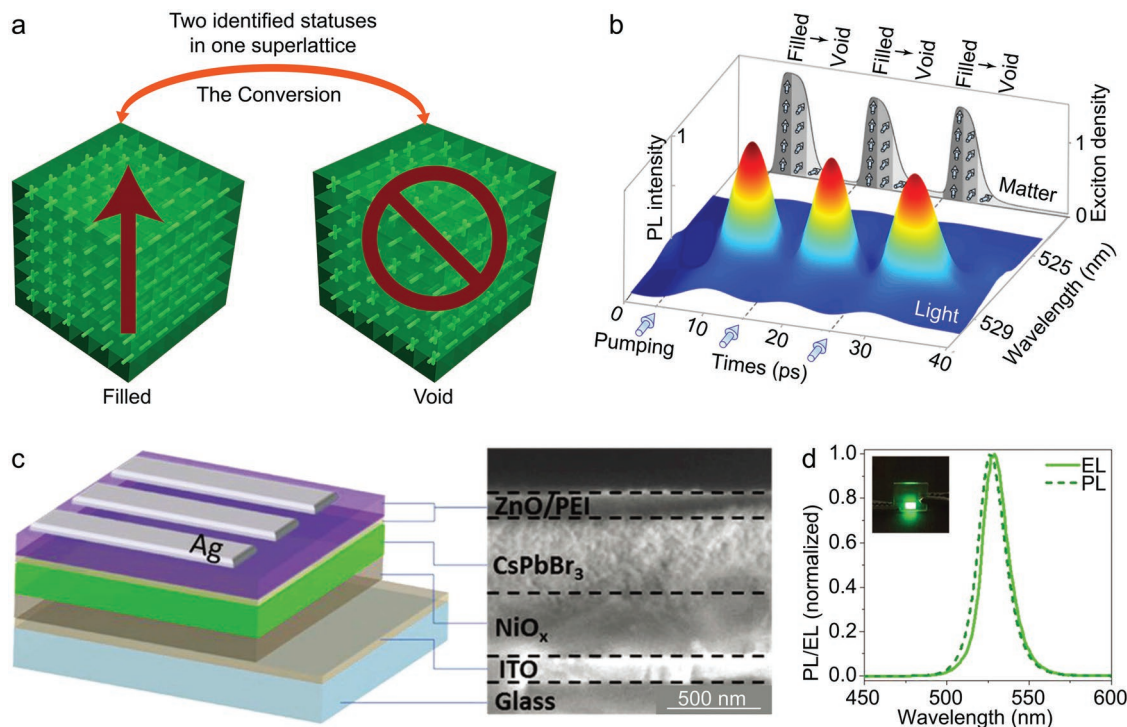


Figure 11. Applications of metal–halide perovskite superlattices. a) Schematic of “filled” and “void” states for perovskite superlattices as quantum containers. b) Experimental demonstration of a quantum container with an ultrafast conversion of an excitonic quantum ensemble and optical response to microcavity-enhanced superfluorescence signals. c) Device architecture and cross-sectional SEM images of a CsPbBr₃ perovskite LED. d) Electroluminescence and photoluminescence spectra of CsPbBr₃ superlattices. Inset is the corresponding LED device. (b) Reproduced with permission.^[107] Copyright 2020, Springer Nature. (c,d) Reproduced with permission.^[30] Copyright 2018, Wiley-VCH.

(Figure 11b). It is important to note that the aforementioned processes can be repeated stably, ensuring a quite long device lifetime.

4.2. Light-Emitting Diode

A LED is a semiconductor light source that emits light when current passes through it.^[137] LED development began in 1962 with the successful fabrication of the GaAsP red-emitting LED and culminated in 2014 when the blue LED was awarded the Nobel Prize in Physics, paving the way for the mass production of white light LEDs.^[138–140] In the same way that metal–halide perovskite nanocrystals are used as electroluminescent layers, their superlattices can also be used in LEDs.

Metal–halide perovskite superlattice with green emission can be incorporated into standard green-emitting LEDs (Figure 11c).^[30,35] Traditional dispersed CsPbBr₃ nanocrystals usually exhibit blue-green emission at 510–515 nm. When forming superlattices, the redshift results in pure green emission at 530 nm, making them particularly promising for television displays (Figure 11d). These electroluminescent devices can retain their emission up to a voltage of 7 V.

Red-emitting LEDs fabricated with self-assembled CsPbI₃ nanowires showed a high PLQY of 91% due to strong quantum confinement.^[141] Moreover, the low defect density in the assembled nanowire clusters confers an extended lifetime to LEDs. The same assembly strategy has also been applied to synthesize nanowires with carrier lifetimes two orders of magnitude longer than those of pristine nanocrystals, suggesting that the defect concentration can be effectively reduced through assembly.^[142,143]

Recently, geometrically modified perovskite nanocrystal superlattices were synthesized to achieve a high ratio of the horizontal dipole of up to 0.75. Specifically, the optical transitions showed a pronounced preferential horizontal orientation in the as-prepared anisotropic superlattices, thus greatly enhancing the light outcoupling efficiency. As a result, LEDs fabricated with these superlattices exhibited high external quantum efficiency comparable to state-of-the-art organic LEDs.^[144]

5. Outlook

Over the past five years, metal–halide perovskite superlattices have gained growing attention in the halide perovskite field, and numerous related studies have emerged. This research theme has blossomed, thanks to new synthesis methods and in-depth exploration of the underlying photophysical mechanisms. There are, however, still several open questions that need to be urgently addressed. Moreover, their optical properties seem to be underutilized compared with other luminescent materials.

Metal–halide perovskite superlattices are difficult to characterize optically, especially with respect to superfluorescence, since this optical property becomes less prominent with increasing temperature. For example, despite the high intensity of superfluorescence at cryogenic temperatures (e.g., 6 K), the experimental signal is six orders of magnitude weaker than

the theoretical response.^[124] In other words, thermal decoherence is the critical factor responsible for the drastic reduction in superfluorescence, which strongly hinders its practical application. In this context, simulations can be performed to provide insights into the correlation between thermal dephasing of superfluorescence and nanocrystal size.^[124] Superlattices self-assembled from smaller nanocrystals have a much higher thermal decoherence resistance. For example, at the same temperature, superlattices made of 3 nm nanocrystals exhibit four orders of magnitude stronger superfluorescence response than those made of nanocrystals with a 9 nm length. It is hard to obtain nanocrystals with a size of 3 nm, nevertheless, because the growth of metal–halide perovskite nanocrystals is an ultrafast kinetic process that takes place virtually instantly.^[22] As the nanocrystals get smaller, the size discrepancy becomes more apparent, which complicates the self-assembling process.

The second challenge is the low stability of metal–halide perovskite superlattices. These superlattices disassemble gradually into microcrystals and lose their superlattice characteristics, even when stored in vacuum.^[145] Prolonged irradiation of CsPb(Br_xI_{1-x})₃ superlattices causes an irreversible spectral blueshift due to gradual photoinduced I₂ oxidation and sublimation.^[83,146] Stability can be greatly improved by self-assembly from stable low-dimensional metal–halide perovskite nanocrystals such as Cs₂MX₆ (M = Sn, Zr, Te, Hf; X = Cl, Br, I), also circumventing the lead toxicity issues for CsPbX₃.^[147–153]

Another concern is the modulation of emission wavelength in perovskite nanocrystal superlattices. Although visible light emission has been widely reported in perovskite nanocrystal superlattices, violet, UV, and near-infrared (NIR) emissions have not been reported.^[46,47] On the one hand, the synthesis of high-quality perovskite nanocrystals with violet or UV emission such as CsPbCl₃ remains challenging, since the detachment of surface Cl atoms generates halide vacancies and leads to low PLQY.^[154] Researchers have demonstrated that doping can significantly improve the PLQY of perovskite nanocrystals. Doping with Ni²⁺ or Cd²⁺, for example, resulted in violet- and UV-emitting CsPbCl₃ nanocrystals with PLQY near unity and 60.5%, respectively.^[154,155] It is likely that similar results will be obtained in violet- and UV-emitting perovskite nanocrystal superlattices if doping is applied.

Lanthanide incorporation is an effective strategy to achieve NIR emission in perovskite nanocrystals such as CsPb(Cl_xBr_{1-x})₃.^[156–160] However, the corresponding emission intensity and PLQY of lanthanide emitters are extremely low due to the parity-forbidden optical transition, the small doping amount of lanthanides, and the inefficient energy transfer from the perovskite host to the lanthanide emitters.^[161] Recently, NIR emission beyond 1100 nm was observed in two highly stable lead-free perovskite single crystals, Cs₂MoCl₆ and Cs₂WCl₆.^[162] The pronounced Stokes shift was attributed to the formation of bright self-trapping excitons. If their nanocrystals could be synthesized, it would be conceivable to manufacture Cs₂MoCl₆ and Cs₂WCl₆ superlattices. Since self-trapping excitons are generated in individual nanocrystals and insensitive to interfacial interactions, NIR emission would be retained in these nanocrystal superlattices.

In addition, since the emission color of metal–perovskite nanocrystals can be precisely controlled via fast anionic

exchange, other emission colors are highly likely.^[24] It would be exciting if color-changing superlattices could be obtained by direct halogen exchange in the as-formed superlattices.

A superfluorescence laser can be obtained by designing microcavities with favored geometries, in which external laser beams are used to stimulate and amplify the initial superfluorescence.^[163] Nevertheless, finding high-quality light sources remains difficult at present. The high coherence of amplified stimulated superfluorescence lasers in the corresponding aggregates along with the single-photon characteristic of metal-halide perovskite nanocrystals make their superlattices promising light sources for applications mentioned above.

Boson sampling is often used to demonstrate that quantum computers are more effective than classical servers.^[50] However, the inefficiency of single-photon sources constitutes an obstacle to high-performance boson sampling.^[164–166] Single-photon efficiency is currently limited to 33.7%. Cross-polarization is always present in a working device, reducing the single-photon efficiency up to half.^[167] The single-photon efficiency of superfluorescence lasers from metal-halide perovskite superlattices is expected to be much higher than that of quantum dot-microcavity structures due to their greater coherence than previously mentioned single-photon sources. To achieve higher Boson sampling efficiency, metal-halide perovskites are expected to replace traditional single photon sources. With breakthroughs in detection efficiency, quantum computers of the future will be more powerful than ever before.

Quantum teleportation across large distances has real application value in quantum communications.^[51] Although it is possible to achieve ultralong distance quantum communication over 500 km, studies on nationwide or even global quantum teleportation networks continue. The primary cause is that intercity quantum communication generally involves significant photon loss and decoherence in optical fibers, severely limiting the transmission distance.^[168] Considering that metal-halide perovskite superlattices can serve as bright, coherent light sources, photon loss and light attenuation during quantum teleportation are expected to be less prominent, prolonging the transmission distance.^[169,170]

The use of metal-halide perovskite superlattices in photonic integrated circuits could also be considered.^[52] As with electronic circuits, photons can be generated, transported, captured, and analyzed in photonic integrated circuits. One of the great improvements that can be made from such photonic circuits to next-generation products is to use single photons or highly coherent light in the circuits. Metal-halide perovskite superlattices can work as cavity-coupled quantum emitters that transmit optical signals throughout the entire photonic circuit.^[171] This leads to miniaturization of circuits and much higher data processing efficiency, since light travels faster than electrons. Moreover, the shorter transmission path for photons reduces optical losses, thereby enhancing operation efficiency and extending service life span.

Coherent superfluorescence lasers produced from metal-halide superlattices can also be used in other quantum technologies, such as the investigation of multidimensional quantum walks, the verification of Bell's inequality, and ultimate studies of quantum entanglement.^[172,173] Metal-halide perovskite superlattices are likely to be explored further by researchers

with diverse backgrounds, including materials science, chemistry, computer science, and quantum physics.

Acknowledgements

The authors thank the National Research Foundation (NRF), the Prime Minister's Office of Singapore under its Competitive Research Program (CRP Award No. NRF-CRP23-2019-0002), the NRF Investigatorship Programme (Award No. NRF-NRFI05-2019-0003), and the King Abdullah University of Science and Technology (KAUST) Office of Sponsored Research (OSR) under Award No. OSR-2018-CRG7-3736.

Conflict of Interest

The authors declare no conflict of interest.

Keywords

capping ligands, packing models, perovskite nanocrystals, quantum technology, self-assembly, superfluorescence, superlattices

Received: October 9, 2022

Revised: January 7, 2023

Published online: February 20, 2023

- [1] M. A. Boles, M. Engel, D. V. Talapin, *Chem. Rev.* **2016**, *116*, 11220.
- [2] K. Deng, Z. Luo, L. Tan, Z. Quan, *Chem. Soc. Rev.* **2020**, *49*, 6002.
- [3] M. Scheibner, T. Schmidt, L. Worschech, A. Forchel, G. Bacher, T. Passow, D. Hommel, *Nat. Phys.* **2007**, *3*, 106.
- [4] W. Koh, S. R. Saudari, A. T. Fafarman, C. R. Kagan, C. B. Murray, *Nano Lett.* **2011**, *11*, 4764.
- [5] S. J. Oh, N. E. Berry, J.-H. Choi, E. A. Gaubling, H. Lin, T. Paik, B. T. Diroll, S. Muramoto, C. B. Murray, C. R. Kagan, *Nano Lett.* **2014**, *14*, 1559.
- [6] K. J. Si, D. Sikdar, Y. Chen, F. Eftekhari, Z. Xu, Y. Tang, W. Xiong, P. Guo, S. Zhang, Y. Lu, Q. Bao, W. Zhu, M. Premaratne, W. Cheng, *ACS Nano* **2014**, *8*, 11086.
- [7] P. Podsiadlo, B. Lee, V. B. Prakapenka, G. V. Krylova, R. D. Schaller, A. Demortière, E. V. Shevchenko, *Nano Lett.* **2011**, *11*, 579.
- [8] L. Wu, P.-O. Jubert, D. Berman, W. Imano, A. Nelson, H. Zhu, S. Zhang, S. Sun, *Nano Lett.* **2014**, *14*, 3395.
- [9] N. Liakakos, T. Blon, C. Achkar, V. Vilar, B. Cormary, R. P. Tan, O. Benamara, G. Chaboussant, F. Ott, B. Warot-Fonrose, E. Snoeck, B. Chaudret, K. Soulantica, M. Respaud, *Nano Lett.* **2014**, *14*, 3481.
- [10] Y. Yamada, C.-K. Tsung, W. Huang, Z. Huo, S. E. Habas, T. Soejima, C. E. Aliaga, G. A. Somorjai, P. Yang, *Nat. Chem.* **2011**, *3*, 372.
- [11] Y. Lei, Y. Li, C. Lu, Q. Yan, Y. Wu, F. Babbe, H. Gong, S. Zhang, J. Zhou, R. Wang, R. Zhang, Y. Chen, H. Tsai, Y. Gu, H. Hu, Y.-H. Lo, W. Nie, T. Lee, J. Luo, K. Yang, K.-I. Jang, S. Xu, *Nature* **2022**, *608*, 317.
- [12] B. Zheng, J. Fan, B. Chen, X. Qin, J. Wang, F. Wang, R. Deng, X. Liu, *Chem. Rev.* **2022**, *122*, 5519.
- [13] C. B. Murray, C. R. Kagan, M. G. Bawendi, *Science* **1995**, *270*, 1335.
- [14] P. Jiang, J. F. Bertone, K. S. Hwang, V. L. Colvin, *Chem. Mater.* **1999**, *11*, 2132.
- [15] F. X. Redl, K.-S. Cho, C. B. Murray, S. O'Brien, *Nature* **2003**, *423*, 968.

- [16] E. V. Shevchenko, D. V. Talapin, N. A. Kotov, S. O'Brien, C. B. Murray, *Nature* **2006**, 439, 55.
- [17] X. Ye, J. Chen, M. E. Irrgang, M. Engel, A. Dong, S. C. Glotzer, C. B. Murray, *Nat. Mater.* **2017**, 16, 214.
- [18] X. Li, X. Liu, X. Liu, *Chem. Soc. Rev.* **2021**, 50, 2074.
- [19] U. Landman, W. D. Luedtke, *Faraday Discuss.* **2004**, 125, 1.
- [20] X. Zhang, L. Lv, L. Ji, G. Guo, L. Liu, D. Han, B. Wang, Y. Tu, J. Hu, D. Yang, A. Dong, *J. Am. Chem. Soc.* **2016**, 138, 3290.
- [21] G. Singh, H. Chan, A. Baskin, E. Gelman, N. Reprin, P. Král, R. Klajn, *Science* **2014**, 345, 1149.
- [22] L. Protesescu, S. Yakunin, M. I. Bodnarchuk, F. Krieg, R. Caputo, C. H. Hendon, R. X. Yang, A. Walsh, M. V. Kovalenko, *Nano Lett.* **2015**, 15, 3692.
- [23] M. A. Becker, R. Vaxenburg, G. Nedelcu, P. C. Sercel, A. Shabaev, M. J. Mehl, J. G. Michopoulos, S. G. Lambrakos, N. Bernstein, J. L. Lyons, T. Stöferle, R. F. Mahrt, M. V. Kovalenko, D. J. Norris, G. Rainò, A. L. Efron, *Nature* **2018**, 553, 189.
- [24] G. Nedelcu, L. Protesescu, S. Yakunin, M. I. Bodnarchuk, M. J. Grotevent, M. V. Kovalenko, *Nano Lett.* **2015**, 15, 5635.
- [25] M. V. Kovalenko, L. Protesescu, M. I. Bodnarchuk, *Science* **2017**, 358, 745.
- [26] Q. Chen, J. Wu, X. Ou, B. Huang, J. Almutlaq, A. A. Zhumekenov, X. Guan, S. Han, L. Liang, Z. Yi, J. Li, X. Xie, Y. Wang, Y. Li, D. Fan, D. B. L. Teh, A. H. All, O. F. Mohammed, O. M. Bakr, T. Wu, M. Bettinelli, H. Yang, W. Huang, X. Liu, *Nature* **2018**, 561, 88.
- [27] L. C. Schmidt, A. Pertegás, S. González-Carrero, O. Malinkiewicz, S. Agouran, G. Mínguez Espallargas, H. J. Bolink, R. E. Galian, J. Pérez-Prieto, *J. Am. Chem. Soc.* **2014**, 136, 850.
- [28] A. Dey, J. Ye, A. De, E. Debroye, S. K. Ha, E. Bladt, A. S. Kshirsagar, Z. Wang, J. Yin, Y. Wang, L. N. Quan, F. Yan, M. Gao, X. Li, J. Shamsi, T. Debnath, M. Cao, M. A. Scheel, S. Kumar, J. A. Steele, M. Gerhard, L. Chouhan, K. Xu, X. Wu, Y. Li, Y. Zhang, A. Dutta, C. Han, I. Vincon, A. L. Rogach, et al., *ACS Nano* **2021**, 15, 10775.
- [29] Y. Tong, B. J. Bohn, E. Bladt, K. Wang, P. Müller-Buschbaum, S. Bals, A. S. Urban, L. Polavarapu, J. Feldmann, *Angew. Chem., Int. Ed.* **2017**, 56, 13887.
- [30] Y. Tong, E.-P. Yao, A. Manzi, E. Bladt, K. Wang, M. Döblinger, S. Bals, P. Müller-Buschbaum, A. S. Urban, L. Polavarapu, J. Feldmann, *Adv. Mater.* **2018**, 30, 1801117.
- [31] T. Sugaya, T. Amano, M. Mori, S. Niki, *Appl. Phys. Lett.* **2010**, 97, 043112.
- [32] J. Zhang, A. A. Lutich, A. S. Sussha, M. Döblinger, C. Mauser, A. O. Govorov, A. L. Rogach, F. Jäckel, J. Feldmann, *J. Appl. Phys.* **2010**, 107, 123516.
- [33] M. V. Kovalenko, M. I. Bodnarchuk, *Chimia* **2017**, 71, 461.
- [34] Y. Zhang, T. Shah, F. L. Deepak, B. A. Korgel, *Chem. Mater.* **2019**, 31, 7962.
- [35] E. Cao, J. Qiu, D. Zhou, Y. Yang, Q. Wang, Y. Wen, *Chem. Commun.* **2020**, 56, 4460.
- [36] G. C. Adhikari, P. A. Vargas, H. Zhu, A. Grigoriev, P. Zhu, *Nanoscale Adv.* **2019**, 1, 1791.
- [37] Y. Dong, T. Qiao, D. Kim, D. Parobek, D. Rossi, D. H. Son, *Nano Lett.* **2018**, 18, 3716.
- [38] Y. Bekenstein, J. C. Dahl, J. Huang, W. T. Osowiecki, J. K. Swabeck, E. M. Chan, P. Yang, A. P. Alivisatos, *Nano Lett.* **2018**, 18, 3502.
- [39] Y. Zhang, T. D. Siegler, C. J. Thomas, M. K. Abney, T. Shah, A. De Gorostiza, R. M. Greene, B. A. Korgel, *Chem. Mater.* **2020**, 32, 5410.
- [40] S. K. Mehetor, H. Ghosh, N. Pradhan, *ACS Energy Lett.* **2019**, 4, 1437.
- [41] Y. Nagaoka, K. Hills-Kimball, R. Tan, R. Li, Z. Wang, O. Chen, *Adv. Mater.* **2017**, 29, 1606666.
- [42] C. B. Murray, C. R. Kagan, M. G. Bawendi, *Annu. Rev. Mater. Sci.* **2000**, 30, 545.
- [43] Y. Tang, L. Gomez, A. Lesage, E. Marino, T. E. Kodger, J.-M. Meijer, P. Kolpakov, J. Meng, K. Zheng, T. Gregorkiewicz, P. Schall, *Nano Lett.* **2020**, 20, 5997.
- [44] Y. Ji, M. Wang, Z. Yang, H. Wang, M. A. Padiyar, H. Qiu, J. Dang, Y. Miao, Y. Zhou, A. S. Bhatti, *Nanoscale* **2022**, 14, 2359.
- [45] C. J. Thomas, Y. Zhang, A. Guillaussier, K. Bdeir, O. F. Aly, H. G. Kim, J. Noh, L. C. Reimnitz, J. Li, F. L. Deepak, D.-M. Smilgies, D. J. Milliron, B. A. Korgel, *Chem. Mater.* **2019**, 31, 9750.
- [46] Y. Zhang, C. J. Thomas, A. Guillaussier, D.-M. Smilgies, B. A. Korgel, *J. Phys. Chem. C* **2019**, 123, 17555.
- [47] G. Rainò, M. A. Becker, M. I. Bodnarchuk, R. F. Mahrt, M. V. Kovalenko, T. Stöferle, *Nature* **2018**, 563, 671.
- [48] R. Bonifacio, L. A. Lugiatto, *Phys. Rev. A* **1975**, 11, 1507.
- [49] I. Cherniukh, G. Rainò, T. Stöferle, M. Burian, A. Travesset, D. Naumenko, H. Amenitsch, R. Erni, R. F. Mahrt, M. I. Bodnarchuk, M. V. Kovalenko, *Nature* **2021**, 593, 535.
- [50] H.-S. Zhong, H. Wang, Y.-H. Deng, M.-C. Chen, L.-C. Peng, Y.-H. Luo, J. Qin, D. Wu, X. Ding, Y. Hu, P. Hu, X.-Y. Yang, W.-J. Zhang, H. Li, Y. Li, X. Jiang, L. Gan, G. Yang, L. You, Z. Wang, L. Li, N.-L. Liu, C.-Y. Lu, J.-W. Pan, *Science* **2020**, 370, 1460.
- [51] J. Yin, J.-G. Ren, H. Lu, Y. Cao, H.-L. Yong, Y.-P. Wu, C. Liu, S.-K. Liao, F. Zhou, Y. Jiang, X.-D. Cai, P. Xu, G.-S. Pan, J.-J. Jia, Y.-M. Huang, H. Yin, J.-Y. Wang, Y.-A. Chen, C.-Z. Peng, J.-W. Pan, *Nature* **2012**, 488, 185.
- [52] J. B. Spring, B. J. Metcalf, P. C. Humphreys, W. S. Kolthammer, X.-M. Jin, M. Barbieri, A. Datta, N. Thomas-Peter, N. K. Langford, D. Kundys, J. C. Gates, B. J. Smith, P. G. R. Smith, I. A. Walmsley, *Science* **2013**, 339, 798.
- [53] P. Schapotschnikow, R. Pool, T. J. H. Vlugt, *Mol. Phys.* **2007**, 105, 3177.
- [54] P. Schapotschnikow, R. Pool, T. J. H. Vlugt, *Nano Lett.* **2008**, 8, 2930.
- [55] P. Schapotschnikow, T. J. H. Vlugt, *J. Chem. Phys.* **2009**, 131, 124705.
- [56] M. A. Boles, D. V. Talapin, *J. Am. Chem. Soc.* **2015**, 137, 4494.
- [57] A. Travesset, *Soft Matter* **2017**, 13, 147.
- [58] A. Travesset, *ACS Nano* **2017**, 11, 5375.
- [59] I. Coropceanu, M. A. Boles, D. V. Talapin, *J. Am. Chem. Soc.* **2019**, 141, 5728.
- [60] L. Wu, J. J. Willis, I. S. McKay, B. T. Diroll, J. Qin, M. Cargnello, C. J. Tassone, *Nature* **2017**, 548, 197.
- [61] A. Jana, A. Meena, S. A. Patil, Y. Jo, S. Cho, Y. Park, V. G. Sree, H. Kim, H. Im, R. A. Taylor, *Prog. Mater. Sci.* **2022**, 129, 100975.
- [62] R. L. Whetten, M. N. Shafiqullin, J. T. Khoury, T. G. Schaaff, I. Vezmar, M. M. Alvarez, A. Wilkinson, *Acc. Chem. Res.* **1999**, 32, 397.
- [63] B. K. Patra, H. Agrawal, J.-Y. Zheng, X. Zha, A. Travesset, E. C. Garnett, *ACS Appl. Mater. Interfaces* **2020**, 12, 31764.
- [64] J. R. Heath, C. M. Knobler, D. V. Leff, *J. Phys. Chem. B* **1997**, 101, 189.
- [65] W. M. Gelbart, R. P. Sear, J. R. Heath, S. Chaney, *Faraday Discuss.* **1999**, 112, 299.
- [66] J. N. Israelachvili, *Intermolecular and Surface Forces*, Elsevier Science, London, England **2011**.
- [67] V. K. Ravi, R. A. Scheidt, A. Nag, M. Kuno, P. V. Kamat, *ACS Energy Lett.* **2018**, 3, 1049.
- [68] A. Pan, M. Jurow, Y. Zhao, F. Qiu, Y. Liu, J. Yang, J. J. Urban, L. He, Y. Liu, *Nanoscale* **2017**, 9, 17688.
- [69] P. V. Kamat, N. Pradhan, K. Schanze, P. S. Weiss, J. Buriak, P. Stang, T. W. Odom, G. Hartland, *ACS Energy Lett.* **2020**, 5, 2253.
- [70] V. K. Ravi, R. A. Scheidt, J. DuBose, P. V. Kamat, *J. Am. Chem. Soc.* **2018**, 140, 8887.
- [71] S. K. Mehetor, H. Ghosh, N. Pradhan, *J. Phys. Chem. Lett.* **2019**, 10, 1300.

- [72] M. C. Weidman, M. Seitz, S. D. Stranks, W. A. Tisdale, *ACS Nano* **2016**, *10*, 7830.
- [73] S. Kumar, J. Jagielski, S. Yakunin, P. Rice, Y.-C. Chiu, M. Wang, G. Nedelcu, Y. Kim, S. Lin, E. J. G. Santos, M. V. Kovalenko, C.-J. Shih, *ACS Nano* **2016**, *10*, 9720.
- [74] J. T. Lee, S. Seifert, R. Sardar, *Chem. Mater.* **2021**, *33*, 5917.
- [75] G. C. Adhikari, H. Zhu, P. A. Vargas, P. Zhu, *J. Phys. Chem. C* **2018**, *122*, 15041.
- [76] W. Li, S. Sidhik, B. Traore, R. Asadpour, J. Hou, H. Zhang, A. Fehr, J. Essman, Y. Wang, J. M. Hoffman, I. Spanopoulos, J. J. Crochet, E. Tsai, J. Strzalka, C. Katan, M. A. Alam, M. G. Kanatzidis, J. Even, J.-C. Blancon, A. D. Mohite, *Nat. Nanotechnol.* **2022**, *17*, 45.
- [77] J. Gong, M. Hao, Y. Zhang, M. Liu, Y. Zhou, *Angew. Chem., Int. Ed.* **2022**, *61*, e202112022.
- [78] S. Peng, Z. Wen, T. Ye, X. Xiao, K. Wang, J. Xia, J. Sun, T. Zhang, G. Mei, H. Liu, B. Xu, X. Li, R. Chen, G. Xing, K. Wang, Z. Tang, *ACS Appl. Mater. Interfaces* **2020**, *12*, 31863.
- [79] S. Toso, D. Baranov, C. Giannini, L. Manna, *ACS Nano* **2021**, *15*, 20341.
- [80] M. I. Bodnarchuk, S. C. Boehme, S. ten Brinck, C. Bernasconi, Y. Shynkarenko, F. Krieg, R. Widmer, B. Aeschlimann, D. Günther, M. V. Kovalenko, I. Infante, *ACS Energy Lett.* **2019**, *4*, 63.
- [81] I. Cherniukh, G. Rainò, T. V. Sekh, C. Zhu, Y. Shynkarenko, R. A. John, E. Kobiyama, R. F. Mahrt, T. Stöferle, R. Erni, M. V. Kovalenko, M. I. Bodnarchuk, *ACS Nano* **2021**, *15*, 16488.
- [82] I. Cherniukh, T. V. Sekh, G. Rainò, O. J. Ashton, M. Burian, A. Travesset, M. Athanasiou, A. Manoli, R. A. John, M. Svyrydenko, V. Morad, Y. Shynkarenko, F. Montanarella, D. Naumenko, H. Amenitsch, G. Itkos, R. F. Mahrt, T. Stöferle, R. Erni, M. V. Kovalenko, M. I. Bodnarchuk, *ACS Nano* **2022**, *16*, 7210.
- [83] S. Toso, D. Baranov, L. Manna, *Acc. Chem. Res.* **2021**, *54*, 498.
- [84] F. Krieg, P. C. Sercel, M. Burian, H. Andrusiv, M. I. Bodnarchuk, T. Stöferle, R. F. Mahrt, D. Naumenko, H. Amenitsch, G. Rainò, M. V. Kovalenko, *ACS Cent. Sci.* **2021**, *7*, 135.
- [85] S. Bera, R. K. Behera, N. Pradhan, *J. Am. Chem. Soc.* **2020**, *142*, 20865.
- [86] J. Pan, X. Li, X. Gong, J. Yin, D. Zhou, L. Sinatra, R. Huang, J. Liu, J. Chen, I. Dursun, A. M. El-Zohry, M. I. Saidaminov, H. Sun, O. F. Mohammed, C. Ye, E. H. Sargent, O. M. Bakr, *Angew. Chem., Int. Ed.* **2019**, *58*, 16077.
- [87] D. Jishkariani, K. C. Eibert, Y. Wu, J. D. Lee, M. Hermes, D. Wang, A. van Blaaderen, C. B. Murray, *ACS Nano* **2019**, *13*, 5712.
- [88] M. Imran, P. Ijaz, D. Baranov, L. Goldoni, U. Petralanda, Q. Akkerman, A. L. Abdelhady, M. Prato, P. Bianchini, I. Infante, L. Manna, *Nano Lett.* **2018**, *18*, 7822.
- [89] H. Li, X. Liu, Q. Ying, C. Wang, W. Jia, X. Xing, L. Yin, Z. Lu, K. Zhang, Y. Pan, Z. Shi, L. Huang, D. Jia, *Angew. Chem.* **2020**, *132*, 17360.
- [90] K.-H. Wang, J.-N. Yang, Q.-K. Ni, H.-B. Yao, S.-H. Yu, *Langmuir* **2018**, *34*, 595.
- [91] D. Dong, R. Fu, Q. Shi, W. Cheng, *Nat. Protoc.* **2019**, *14*, 2691.
- [92] M. I. Bodnarchuk, L. Li, A. Fok, S. Nachtergaele, R. F. Ismagilov, D. V. Talapin, *J. Am. Chem. Soc.* **2011**, *133*, 8956.
- [93] N. Soetan, W. R. Erwin, A. M. Tonigan, D. G. Walker, R. Bardhan, *J. Phys. Chem. C* **2017**, *121*, 18186.
- [94] J. Henzie, M. Grünwald, A. Widmer-Cooper, P. L. Geissler, P. Yang, *Nat. Mater.* **2012**, *11*, 131.
- [95] D. V. Talapin, E. V. Shevchenko, C. B. Murray, A. Kornowski, S. Förster, H. Weller, *J. Am. Chem. Soc.* **2004**, *126*, 12984.
- [96] B. Abécassis, M. D. Tessier, P. Davidson, B. Dubertret, *Nano Lett.* **2014**, *14*, 710.
- [97] D. Lapkin, C. Kirsch, J. Hiller, D. Andrienko, D. Assalauova, K. Braun, J. Carnis, Y. Y. Kim, M. Mandal, A. Maier, A. J. Meixner, N. Mukharamova, M. Scheele, F. Schreiber, M. Sprung, J. Wahl, S. Westendorf, I. A. Zaluzhnyy, I. A. Vartanyants, *Nat. Commun.* **2022**, *13*, 892.
- [98] Z. Zhang, S. Ghimire, T. Okamoto, B. M. Sachith, J. Sobhanan, C. Subrahmanyam, V. Biju, *ACS Nano* **2022**, *16*, 160.
- [99] J. S. van der Burgt, J. J. Geuchies, B. van der Meer, H. Vanrompay, D. Zanaga, Y. Zhang, W. Albrecht, A. V. Petukhov, L. Fillion, S. Bals, I. Swart, D. Vanmaekelbergh, *J. Phys. Chem. C* **2018**, *122*, 15706.
- [100] A. Jana, Y. Jo, H. Im, *Matter* **2021**, *4*, 2607.
- [101] Y. Kim, E. Yassitepe, O. Voznyy, R. Comin, G. Walters, X. Gong, P. Kanjanaboos, A. F. Nogueira, E. H. Sargent, *ACS Appl. Mater. Interfaces* **2015**, *7*, 25007.
- [102] S. Toso, D. Baranov, D. Altamura, F. Scattarella, J. Dahl, X. Wang, S. Marras, A. P. Alivisatos, A. Singer, C. Giannini, L. Manna, *ACS Nano* **2021**, *15*, 6243.
- [103] F. Bertolotti, A. Vivani, F. Ferri, P. Anzini, A. Cervellino, M. I. Bodnarchuk, G. Nedelcu, C. Bernasconi, M. V. Kovalenko, N. Masciocchi, A. Guagliardi, *Chem. Mater.* **2022**, *34*, 594.
- [104] S. Toso, D. Baranov, C. Giannini, S. Marras, L. Manna, *ACS Mater. Lett.* **2019**, *1*, 272.
- [105] L. Dai, Z. Deng, F. Auras, H. Goodwin, Z. Zhang, J. C. Walmsley, P. D. Bristowe, F. Deschler, N. C. Greenham, *Nat. Photonics* **2021**, *15*, 696.
- [106] Y. Zhou, M. Saliba, *ACS Energy Lett.* **2021**, *6*, 2750.
- [107] C. Zhou, Y. Zhong, H. Dong, W. Zheng, J. Tan, Q. Jie, A. Pan, L. Zhang, W. Xie, *Nat. Commun.* **2020**, *11*, 329.
- [108] Y. Zhong, C. Zhou, L. Hou, J. Li, W. Xie, H. Dong, L. Zhang, *Adv. Opt. Mater.* **2022**, *10*, 2102290.
- [109] Z. Cao, F. Hu, C. Zhang, S. Zhu, M. Xiao, X. Wang, *Adv. Photonics* **2020**, *2*, 054001.
- [110] C. Zhou, J. M. Pina, T. Zhu, D. H. Parmar, H. Chang, J. Yu, F. Yuan, G. Bappi, Y. Hou, X. Zheng, J. Abed, H. Chen, J. Zhang, Y. Gao, B. Chen, Y. Wang, H. Chen, T. Zhang, S. Hoogland, M. I. Saidaminov, L. Sun, O. M. Bakr, H. Dong, L. Zhang, E. H. Sargent, *Adv. Sci.* **2021**, *8*, 2101125.
- [111] D. Baranov, S. Toso, M. Imran, L. Manna, *J. Phys. Chem. Lett.* **2019**, *10*, 655.
- [112] H. Huang, M. W. Feil, S. Fuchs, T. Debnath, A. F. Richter, Y. Tong, L. Wu, Y. Wang, M. Döblinger, B. Nickel, *Chem. Mater.* **2020**, *32*, 8877.
- [113] S. V. Frolov, W. Gellermann, M. Ozaki, K. Yoshino, Z. V. Vardeny, *Phys. Rev. Lett.* **1997**, *78*, 729.
- [114] R. Florian, L. O. Schwan, D. Schmid, *Phys. Rev. A* **1984**, *29*, 2709.
- [115] N. Skribanowitz, I. P. Herman, J. C. MacGillivray, M. S. Feld, *Phys. Rev. Lett.* **1973**, *30*, 309.
- [116] R. H. Dicke, *Phys. Rev.* **1954**, *93*, 99.
- [117] A. E. Siegman, *Lasers*, University Science Books, Mill Valley, CA, USA **1986**.
- [118] M. Gross, S. Haroche, *Phys. Rep.* **1982**, *93*, 301.
- [119] S. L. McCall, A. F. J. Levi, R. E. Slusher, S. J. Pearton, R. A. Logan, *Appl. Phys. Lett.* **1992**, *60*, 289.
- [120] Y. Deok Jeong, Y. Hyub Won, S. Ook Choi, J. Hyun Yoon, *Opt. Lett.* **2006**, *31*, 2586.
- [121] D. Bates, B. Bederson, *Advances in Atomic and Molecular Physics*, Academic Press, New York **1981**.
- [122] M. G. Benedict, *Super-Radiance: Multiatomic Coherent Emission*, IOP Publishing, Bristol and Philadelphia **1996**.
- [123] D. C. Burnham, R. Y. Chiao, *Phys. Rev.* **1969**, *188*, 667.
- [124] F. Mattiotti, M. Kuno, F. Borgonovi, B. Jankó, G. L. Celardo, *Nano Lett.* **2020**, *20*, 7382.
- [125] G. Findik, M. Biliroglu, D. Seyitliyev, J. Mendes, A. Barrette, H. Ardekani, L. Lei, Q. Dong, F. So, K. Gundogdu, *Nat. Photonics* **2021**, *15*, 676.
- [126] M. Biliroglu, G. Findik, J. Mendes, D. Seyitliyev, L. Lei, Q. Dong, Y. Mehta, V. V. Temnov, F. So, K. Gundogdu, *Nat. Photonics* **2022**, *16*, 324.

- [127] A. Einstein, *Phys. Z.* **1917**, *18*, 124.
- [128] G. L. Lippi, *Atoms* **2021**, *9*, 6.
- [129] M. S. Malcuit, J. J. Maki, D. J. Simkin, R. W. Boyd, *Phys. Rev. Lett.* **1987**, *59*, 1189.
- [130] O. Vybornyi, S. Yakunin, M. V. Kovalenko, *Nanoscale* **2016**, *8*, 6278.
- [131] Y. Tang, D. Poonia, M. van der Laan, D. Timmerman, S. Kinge, L. D. A. Sibbeles, P. Schall, *ACS Appl. Energy Mater.* **2022**, *5*, 5415.
- [132] D. Vila-Liarte, M. W. Feil, A. Manzi, J. L. Garcia-Pomar, H. Huang, M. Döblinger, L. M. Liz-Marzán, J. Feldmann, L. Polavarapu, A. Mihi, *Angew. Chem., Int. Ed.* **2020**, *59*, 17750.
- [133] Y. Gao, E. Shi, S. Deng, S. B. Shiring, J. M. Snaider, C. Liang, B. Yuan, R. Song, S. M. Janke, A. Liebman-Peláez, P. Yoo, M. Zeller, B. W. Boudouris, P. Liao, C. Zhu, V. Blum, Y. Yu, B. M. Savoie, L. Huang, L. Dou, *Nat. Chem.* **2019**, *11*, 1151.
- [134] N. Wang, L. Cheng, R. Ge, S. Zhang, Y. Miao, W. Zou, C. Yi, Y. Sun, Y. Cao, R. Yang, Y. Wei, Q. Guo, Y. Ke, M. Yu, Y. Jin, Y. Liu, Q. Ding, D. Di, L. Yang, G. Xing, H. Tian, C. Jin, F. Gao, R. H. Friend, J. Wang, W. Huang, *Nat. Photonics* **2016**, *10*, 699.
- [135] J. Jagielski, S. Kumar, M. Wang, D. Scullion, R. Lawrence, Y.-T. Li, S. Yakunin, T. Tian, M. V. Kovalenko, Y.-C. Chiu, E. J. G. Santos, S. Lin, C.-J. Shih, *Sci. Adv.* **2017**, *3*, eaaq0208.
- [136] J. Jagielski, S. F. Solari, L. Jordan, D. Scullion, B. Blülle, Y.-T. Li, F. Krumeich, Y.-C. Chiu, B. Ruhstaller, E. J. G. Santos, C.-J. Shih, *Nat. Commun.* **2020**, *11*, 387.
- [137] P. Sharma, M. Khan, A. Choubey, *Int. J. Eng. Technol.* **2019**, *6*, 6486.
- [138] R. D. Dupuis, M. R. Krames, *J. Lightwave Technol.* **2008**, *26*, 1154.
- [139] S. Nakamura, T. Mukai, M. Senoh, *Appl. Phys. Lett.* **1994**, *64*, 1687.
- [140] Y. Nanishi, *Nat. Photonics* **2014**, *8*, 884.
- [141] C. Bi, J. Hu, Z. Yao, Y. Lu, D. Binks, M. Sui, J. Tian, *Adv. Funct. Mater.* **2020**, *30*, 2005990.
- [142] J. Liu, K. Song, Y. Shin, X. Liu, J. Chen, K. X. Yao, J. Pan, C. Yang, J. Yin, L.-J. Xu, H. Yang, A. M. El-Zohry, B. Xin, S. Mitra, M. N. Hedhili, I. S. Roqan, O. F. Mohammed, Y. Han, O. M. Bakr, *Chem. Mater.* **2019**, *31*, 6642.
- [143] J. Liu, X. Zheng, O. F. Mohammed, O. M. Bakr, *Acc. Chem. Res.* **2022**, *55*, 262.
- [144] S. Kumar, T. Marcato, F. Krumeich, Y.-T. Li, Y.-C. Chiu, C.-J. Shih, *Nat. Commun.* **2022**, *13*, 2106.
- [145] D. Baranov, A. Fieramosca, R. X. Yang, L. Polimeno, G. Lerario, S. Toso, C. Giansante, M. D. Giorgi, L. Z. Tan, D. Sanvitto, L. Manna, *ACS Nano* **2021**, *15*, 650.
- [146] M. C. Brennan, S. Toso, I. M. Pavlovets, M. Zhukovskiy, S. Marras, M. Kuno, L. Manna, D. Baranov, *ACS Energy Lett.* **2020**, *5*, 1465.
- [147] S. Liu, B. Yang, J. Chen, D. Zheng, Z. Tang, W. Deng, K. Han, *Laser Photonics Rev.* **2022**, *16*, 2100439.
- [148] Z. Tan, Y. Chu, J. Chen, J. Li, G. Ji, G. Niu, L. Gao, Z. Xiao, J. Tang, *Adv. Mater.* **2020**, *32*, 2002443.
- [149] Z. Tan, J. Li, C. Zhang, Z. Li, Q. Hu, Z. Xiao, T. Kamiya, H. Hosono, G. Niu, E. Lifshitz, Y. Cheng, J. Tang, *Adv. Funct. Mater.* **2018**, *28*, 1801131.
- [150] T. Chang, Q. Wei, R. Zeng, S. Cao, J. Zhao, B. Zou, *J. Phys. Chem. Lett.* **2021**, *12*, 1829.
- [151] W. Ke, M. G. Kanatzidis, *Nat. Commun.* **2019**, *10*, 965.
- [152] A. Babayigit, A. Ethirajan, M. Muller, B. Conings, *Nat. Mater.* **2016**, *15*, 247.
- [153] M. Wang, J. Lyu, X. Qin, S.-W. Yang, X. Liu, G. Q. Xu, *J. Phys. Chem. Lett.* **2022**, *13*, 9429.
- [154] Z.-J. Yong, S.-Q. Guo, J.-P. Ma, J.-Y. Zhang, Z.-Y. Li, Y.-M. Chen, B.-B. Zhang, Y. Zhou, J. Shu, J.-L. Gu, L.-R. Zheng, O. M. Bakr, H.-T. Sun, *J. Am. Chem. Soc.* **2018**, *140*, 9942.
- [155] Y. Zhang, X. Cheng, D. Tu, Z. Gong, R. Li, Y. Yang, W. Zheng, J. Xu, S. Deng, X. Chen, *Angew. Chem., Int. Ed.* **2021**, *60*, 9693.
- [156] G. Pan, X. Bai, D. Yang, X. Chen, P. Jing, S. Qu, L. Zhang, D. Zhou, J. Zhu, W. Xu, B. Dong, H. Song, *Nano Lett.* **2017**, *17*, 8005.
- [157] T. J. Milstein, K. T. Kluherz, D. M. Kroupa, C. S. Erickson, J. J. De Yoreo, D. R. Gamelin, *Nano Lett.* **2019**, *19*, 1931.
- [158] T. J. Milstein, D. M. Kroupa, D. R. Gamelin, *Nano Lett.* **2018**, *18*, 3792.
- [159] D. Zhou, R. Sun, W. Xu, N. Ding, D. Li, X. Chen, G. Pan, X. Bai, H. Song, *Nano Lett.* **2019**, *19*, 6904.
- [160] X. Luo, T. Ding, X. Liu, Y. Liu, K. Wu, *Nano Lett.* **2019**, *19*, 338.
- [161] J.-C. G. Bünzli, V. K. Pecharsky, *Handbook on the Physics and Chemistry of Rare Earths*, North-Holland Publishing Company, Amsterdam **2022**.
- [162] Z. Liu, X. Qin, Q. Chen, Q. Chen, Y. Jing, Z. Zhou, Y. S. Zhao, J. Chen, X. Liu, *Adv. Opt. Mater.* **2022**, *10*, 2201254.
- [163] J. Shamsi, G. Rainò, M. V. Kovalenko, S. D. Stranks, *Nat. Nanotechnol.* **2021**, *16*, 1164.
- [164] M. A. Broome, A. Fedrizzi, S. Rahimi-Keshari, J. Dove, S. Aaronson, T. C. Ralph, A. G. White, *Science* **2013**, *339*, 794.
- [165] M. Tillmann, B. Dakić, R. Heilmann, S. Nolte, A. Szameit, P. Walther, *Nat. Photonics* **2013**, *7*, 540.
- [166] M. Bentivegna, N. Spagnolo, C. Vitelli, F. Flamini, N. Viggianiello, L. Latmiral, P. Mataloni, D. J. Brod, E. F. Galvão, A. Crespi, R. Ramponi, R. Osellame, F. Sciarrino, *Sci. Adv.* **2015**, *1*, e1400255.
- [167] H. Wang, Y. He, Y.-H. Li, Z.-E. Su, B. Li, H.-L. Huang, X. Ding, M.-C. Chen, C. Liu, J. Qin, J.-P. Li, Y.-M. He, C. Schneider, M. Kamp, C.-Z. Peng, S. Höfling, C.-Y. Lu, J.-W. Pan, *Nat. Photonics* **2017**, *11*, 361.
- [168] J.-P. Chen, C. Zhang, Y. Liu, C. Jiang, W.-J. Zhang, Z.-Y. Han, S.-Z. Ma, X.-L. Hu, Y.-H. Li, H. Liu, F. Zhou, H.-F. Jiang, T.-Y. Chen, H. Li, L.-X. You, Z. Wang, X.-B. Wang, Q. Zhang, J.-W. Pan, *Nat. Photonics* **2021**, *15*, 570.
- [169] C. H. Bennett, G. Brassard, *Theor. Comput. Sci.* **2014**, *560*, 7.
- [170] C. H. Bennett, F. Bessette, G. Brassard, L. Salvail, J. Smolin, *J. Cryptol.* **1992**, *5*, 3.
- [171] E. Pelucchi, G. Fagas, I. Aharonovich, D. Englund, E. Figueroa, Q. Gong, H. Hannes, J. Liu, C.-Y. Lu, N. Matsuda, J.-W. Pan, F. Schreck, F. Sciarrino, C. Silberhorn, J. Wang, K. D. Jöns, *Nat. Rev. Phys.* **2022**, *4*, 194.
- [172] H. Tang, X.-F. Lin, Z. Feng, J.-Y. Chen, J. Gao, K. Sun, C.-Y. Wang, P.-C. Lai, X.-Y. Xu, Y. Wang, L.-F. Qiao, A.-L. Yang, X.-M. Jin, *Sci. Adv.* **2018**, *4*, eaat3174.
- [173] R. Horodecki, P. Horodecki, M. Horodecki, K. Horodecki, *Rev. Mod. Phys.* **2009**, *81*, 865.



Zhuang Liu earned his B.E. degree (2016) in Metallic Materials and Engineering and M.S. degree (2019) in Materials Science from the Sichuan University, P. R. China. He is currently pursuing his Ph.D. in Chemistry at the National University of Singapore under the supervision of Prof. Xiaogang Liu. His research interest lies in developing novel metal–halide perovskite materials and expanding their applications.



Xian Qin is a Senior Research Fellow in the Department of Chemistry at the National University of Singapore. She earned her B.S. degree in Mechanical Engineering from the Sichuan University and received her Ph.D. from the Harbin Institute of Technology in 2013. She subsequently conducted postdoctoral training at the National University of Singapore and the Institute of Materials Research and Engineering, Singapore. Her current research agenda is focused on the convergence of multiple areas of expertise, including molecular optoelectronics, energy conversion material design, nanocatalysis, and a deep understanding of the photophysical processes of luminescent nanomaterials through quantum calculations and classical simulations.



Qihao Chen obtained his B.S. degree in Chemistry from the Nanjing University in 2018. He is currently a Master's student in the College of Chemistry at the Fuzhou University under the supervision of Prof. Qiushui Chen. His study focuses on the design of photoluminescent inorganic nanomaterials for biomedical applications.



Tianci Jiang earned her B.E. degree in Materials and Chemical Engineering from the Shandong University of Technology in 2021, and she is currently pursuing an M.Sc. in Chemical Engineering under the guidance of Prof. Qiushui Chen at the Fuzhou University. She is conducting a study to understand the energy conversion mechanism of nanoscintillators and explore the potential of these nanophosphors for X-ray luminescence biosensing and imaging.



Qiushui Chen is a Professor in the Department of Chemistry at the Fuzhou University. He received his B.S. degree in Chemistry from the Fuzhou University in 2009 and his Ph.D. in Chemistry from the Tsinghua University in 2014. After completing his doctoral studies, he worked as a Postdoctoral Researcher in Prof. Xiaogang Liu's group in the Department of Chemistry at the National University of Singapore. His research interests center around the development of high-efficiency X-ray luminescence nanocrystals for emerging applications.



Xiaogang Liu earned his Ph.D. (2004) in Inorganic Chemistry from Northwestern University, Evanston, IL, USA and worked as a Postdoctoral Researcher at the Massachusetts Institute of Technology. Currently, he works at the National University of Singapore and holds a joint appointment at the Institute of Materials Research and Engineering. He is an Associate Editor of *Nanoscale* and *BMEMat*. Among his research interests are the study of energy transfer in lanthanide-doped nanomaterials, the application of optical nanomaterials for neuromodulation, the development of advanced X-ray imaging scintillators, and the prototyping of electronic tools for assistive technologies.